PFC/RR-89-15

Final Technical Report on Propulsion Research on the Hybrid Plume Rocket

for the period

September 1, 1988 – August 31, 1989

F. R. Chang-Díaz*

T. F. Yang

MIT Plasma Fusion Center

AFOSR Contract #84-0190

*Astronaut Office of the Johnson Space Center

Abstract

This report discusses the construction of a tandem mirror plasma propulsion facility, the numerical modelling of the hybrid plume exhaust, and rf heating of the plasma. A preliminary experiment of the ICRH (Ion Cyclotron Resonance Heating) heating of plasma ions was carried out. For 2.0 kW ECRH (Electron Cyclotron Resonance Heating) power injected into the central cell and 10 kW ICRH power into the end cell, the results obtained from the probe in the central cell are: $n_e = 2.5 \times 10^{16}$ m^{-3} and $T_e = 80$ eV (928,000 K) in the central cell. The estimated values in the end cell are: $n_I = 1.25 \times 10^{17}$ m^{-3} and $T_I = 500$ eV (5,797,000 K). The power conversion efficiency was about 80%. The results from time dependent 3-D three fluid numerical modeling indicate that a boundary layer can be formed. The formation of this layer is strongly dependent on neutral jet geometry and injection angle. The ICRH heating of plasma was modeled numerically and power absorption efficiency is about 50%. Analytical analyses was done on slab geometry.

1 Concept

A hybrid plume is one in which the exhaust fluid is a stratified mixture of hot plasma and neutral gas in a magnetic field. The macroscopic properties near the wall boundary (i.e., temperature, density, fluid velocity, thrust, etc.) exhibit a drastic radial variation over small distances. The exhaust is extremely hot in the core and relatively cold near the edge [1,2].

Such a hybrid plume can be produced by surrounding the hot plasma exhausted from the end of a tandem mirror magnetic confinement device with an annular hypersonic gas jet coaxial with the plasma or with various pitch angles [3,4,5]. The resulting plasma-gas structure has useful applications in rocket propulsion of wide power levels where I_{sp} and thrust can be continuously varied.

2 Accomplishments

During the past year we have devoted our major effort to the construction of the tandem mirror magnetic plasma confinement device. The device was assembled in a short eight-month period and the facility became operational in March 1989. An overall view of the device is shown in Fig. 1. A microwave created hydrogen plasma has been heated by rf power to a temperature for electrons of 80 eV which translates to 928,000 K and an estimated temperature for ions of 500 eV or the equivalent of 5,797,000 K.

After years of wrestling with numerical instabilities, particle conservation and outflow boundary problems, and result interpretation, meaningful and positive hybrid plume characteristics have been produced by computational modeling. Preliminary results indicate that a boundary layer can be found with proper injection of neutral gas. This reconfirms previous steady state studies but with much more interesting aspects.

2.1 Experimental Facility

The tandem mirror device was built under the instrumentation program with additional support from JPL/NASA. The detailed construction work on the device has been described in the final technical report. It is briefly summarized below.

The tandem mirror plasma rocket experimental device, a scaled down compact version of the fusion device, is very complicated in structure and operation. It involves sophisticated mechanical components, ultra-high and delicate vacuum system, magnetic coil and cryogenic system, high current power supplies, microwave power transmitters, high power and high voltage radio frequency wave power transmitters. The involvement of diagnostic equipment is even more extensive. A Langmuir probe can only take measurements in the edge of the plasma where the temperature is low; it cannot measure ion temperature. More equipment is needed, such as a microwave interferometer for measuring electron density, from which ion density can be inferred assuming charge neutrality; a laser Thomson scattering system or a visible light spectrometer for measuring ion temperature; a particle beam for measuring plasma potential; a laser fluorescence system for measuring neutral

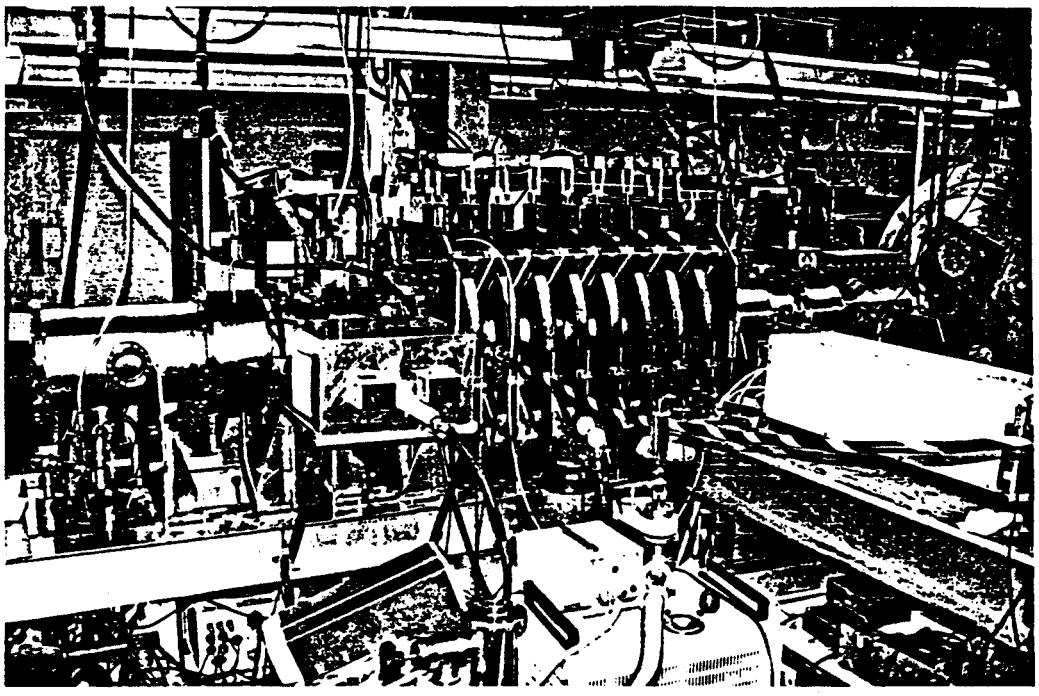

Figure 1, An side view of the Tandem Mirror Plasma Rocket experimental facility.

density, a charge exchange analyzer, retarding field energy analyzers, radiation detectors, diagmagnetic loops, etc. In terms of operation, the pulsing of the magnet, rf, microwave, gas flow and the diagnostic systems have to be synchronized in a proper time sequence. Therefore one of the purposes of this research is to develop methods of simplifying this process. However, every diagnostic is needed to understand the plasma property fully before this can happen. Because of budget constraints and manpower limitations, it will take a long time to gradually build up this capability.

The magnetic coil system and vacuum system were assembled in August 1988. High vacuum was achieved immediately. The magnetic system was operated at low power and microwave discharge was initiated. To reach this point a lot of hard work was involved, such as extensive metal polishing of the coil casing and vacuum chamber, repeated electrical testing of the coil, vacuum testing of the chamber and coil casing, and careful assembly, alignment and calibration of the system.

From September 1988 through January 1989 we worked to complete the construction of the facility. To achieve that the following tasks were done: In our laboratory we constructed a power control unit which was installed and tested. We installed the high current cables. The cryogenic system was installed and tested and a resistance drop of factor 5 was achieved when the coil was cooled down to liquid nitrogen temperature. Two rf transmitter units were brought up to operation. A laser diagnostic system was set up and optical alignment was tested. The end chamber was modified by installing two large rectangular ports and small ports for the implementation of the laser fluorescence system. A second pumping line was installed.

Testing of the system began in February 1989. A giant step was taken in energizing the magnetic coils with high current. Because of the urgent need of bringing the system to full operation rapidly, we took the risk of bringing the current to about 60% of the designed value quickly causing one coil to short. It had to be repaired. The mirror coil set and the set of central cell coils and booster coils are powered by two separate power supplies. The power supplies were found to interfere with each other as shown by the current waveform in Fig. 2a. The power supplies had to be adjusted to obtain the current

(a)

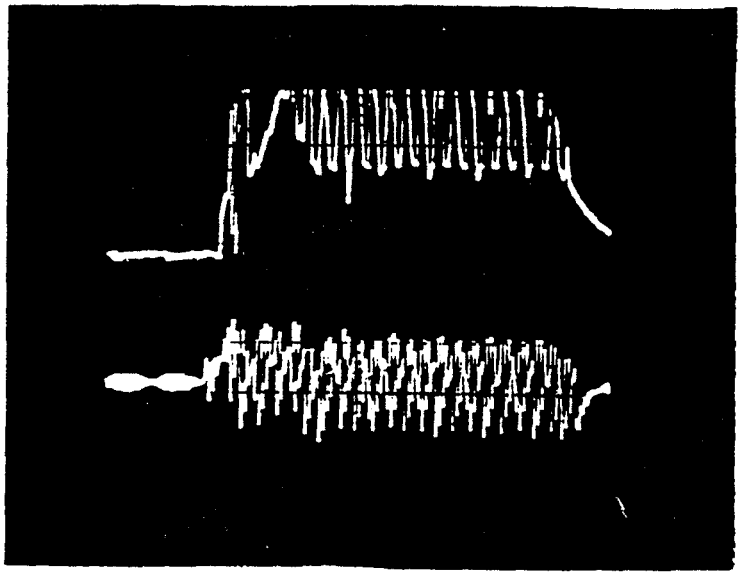

(b)

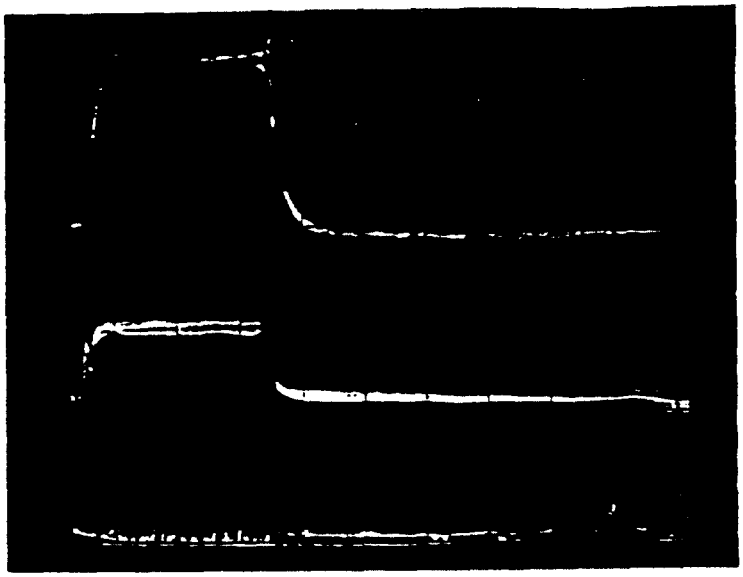

Fig. 2. Current waveforms to the mirror coils (top trace) and central cell (lower trace). (a) Before compensation: (b) after compensation.

waveform in Fig. 2b.

The next step was to inject rf power into the chamber. It was found that the microwave and rf powers could not be operated simultaneously. The microwave is in resonance with electron cyclotron frequency at low magnetic field and rf is in resonance with ion cyclotron frequency at high field. The microwave antenna had to be relocated to the central cell where the field is a factor of 10 lower than the field in the end cell. The end cell antenna was installed in the center plane of the cell which blocked all ports and had to be modified and reinstalled. Accomplishing these two modifications was a major operation because the coils had to be separated. Again due to the race with time, the rf power was injected before the circuit was optimally tuned. The coupler of the transmission line was damaged by arcing from the reflected power. After the system was checked out and repaired, we spent weeks tuning the rf matching circuit. In the meantime a semi-automatic control system was installed. The pulse length of charging the magnet can be limited by a time sequencer to eliminate accidental human error.

The pressure in the chamber was found to be rising too fast during the test. This indicated that an ultra-high vacuum procedure of baking and glow-discharge cleaning had to be taken. This was a long and tedious process which was avoided again in favor of speeding up the program. Also, all the mechanical pumps had to be serviced. All the diagnostics were taken down in order to carry out thorough checking and testing with repetative baking and cleaning to establish a base vacuum condition.

The experience of building such a compact fusion type device might be proven useful in the future for space exploration. It is inheritantly complex and costly. To design, construct and make it operational was quite a challenging task and it is in fact a major part of scientific undertaking.

2.2 Initial Experiment

The plasma heating experiment has been carried out during the testing period by back filling the chamber to a pressure from 5×10^{-5} Torr to 20×10^{-3} Torr at various field intensities, rf power levels and pulse lengths. The only diagnostic we had was the Langmuir probe. The Langmuir probe is a fundamental diagnostics and provides a basic and reliable measurement. However, it has a severe limitation and fundamental difficulties. One has to be very careful to prove that the measurement is correct. The fundamental limitation is that the probe comes in contact with the plasma and it can be burned easily. The probe can also pick up any electrical noise, fluctuations and is particularly susceptible to the interference of rf power. The result could be very deceiving. For a long time we were skeptical on the probe measurements. Such prudence was proved to be correct as discussed later.

Figure 3a shows the probe measurement of an ECRH discharge. The top trace is the waveform of microwave power injected into the chamber. The middle trace is the probe sweeping voltage waveform. The bottom trace is the probe reading of the plasma. During each sweep the probe signal was found to be modulated by the ECRH power which turned out to be a pulsed system. The plasma was not sustained. A constant source of microwave power is thereore needed. We will modify the unit in the future because we cannot afford to take the risk of shutting down the experiment at the present time.

As shown in Fig. 3b there is a very strong probe signal when rf power was injected. The signal is about a factor of 10 larger than the microwave discharge which is shown by the small ripples on the same baseline. Although we later found that this is much larger than the pickup without plasma, we had doubts that the signal was real. A long study was carried out on the structure of the probe, electrical isolation and shielding, ground loop and filtering until a signal showing the current-voltage characteristics typical of a Langmuir probe was obtained. Such a signal is shown by the second trace in Fig. 4. This gave us confidence in the measurement. The electron temperature can be deduced from

(a)

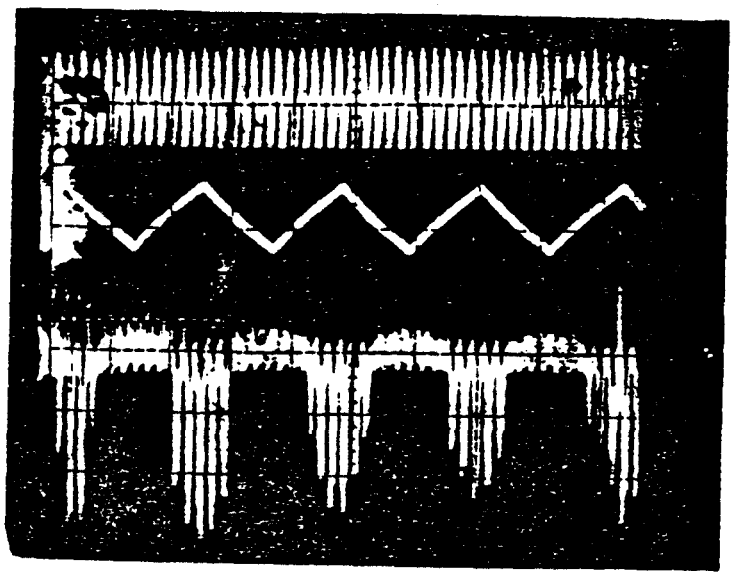

(b)

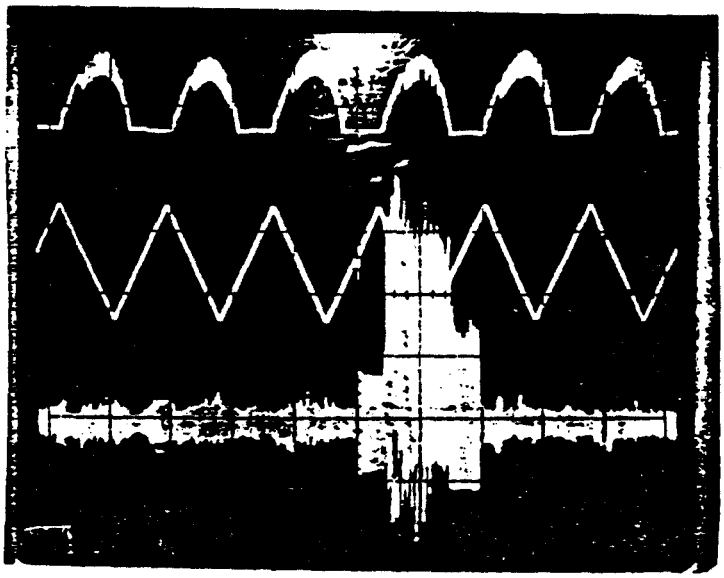

Fig. 3. Langmuir probe measurements of plasma: (a) with microwave discharge; (b) with low power rf heating at 10 ms pulse width. Top and middle traces show microwave and probe sweeping voltages.

Figure 4, The Charateristics of Langmuir probe shown by the middle trace. The top trace is the microve pulse and the bottom trace is probe sweeping voltage.

the following equation [6]

$$T_e = c(I - I_{si}) \Big/ \frac{dI}{dV} \tag{1}$$

where I_{si} is the ion saturation current. The electron density is given approximately by

$$n_e \simeq \frac{I_{si}}{Ae}\sqrt{\frac{m_e}{(T_e)}} \tag{2}$$

where A is the cross sectional area of the probe tip which is a sphere of 2 mm in diameter, T_i is the ion temperature, and e is the charge and mass of electrons.

2.3 Exhaust Modeling

The exhaust modeling has been carried out by solving steady state MHD equations. A time dependent, three fluid (electron, ion and neutral) code by solving transport equations in cylindrical geometry including interactions between species has been developed. We began to learn the dynamic behavior of the plasma-gas system. The theory and the simulation method are described below.

The macroscopic quantities (n,$\mathbf{V}$, and T) are modeled via a fluid representation. The basic equations can be obtained from the work of Braginskii [7]. Braginskii assumed that there was no processes that convert particles of one species to another, so the right hand side of his particle conservation equation, for example, is set to zero. We have such processes, and must generalize the equations appropriately. We need fluid equations for the conservation of particles, momentum, and energy. The equations to be presented will be for the plasma ion species. The equations for electron species are identical. The equations for the neutral gas are the same, except for the momentum conservation equation, which lacks the Lorentz force term. To close the fluid equations, we need an equation of state to specify the relation between pressure and temperature.

The Transport Equations

The equation for conservation of particles is (Eq. (1.11) of Braginskii in reference 7)

$$\frac{\partial n}{\partial t} + \nabla \cdot (n\mathbf{V}) = S_p \ . \tag{3}$$

Here n is the particle density and $\mathbf{V}$ is the mean fluid velocity, defined as

$$\mathbf{V} = \langle \mathbf{v} \rangle \ . \tag{4}$$

$\mathbf{v}$ is the exact particle velocity, and the $\langle \cdot \rangle$ denotes an average over velocity space. S_p is the particle source term, to be described in detail later.

The equation for the conservation of momentum is (Eq. (1.12) of Braginskii in reference 7)

$$\frac{\partial}{\partial t}(mn\mathbf{V}) + \nabla \cdot (mn \langle \mathbf{vv} \rangle) - en\left(\mathbf{E} + \frac{1}{c}\mathbf{V} \times \mathbf{B}\right) = \mathbf{R} \ . \tag{5}$$

Here $\mathbf{v} = \mathbf{v}' + \mathbf{V}$, the exact particle velocity, and $\mathbf{v}'$ is a random velocity.

Ignoring viscosity, this becomes:

$$\frac{\partial}{\partial t}(mn\mathbf{V}) + \nabla \cdot (mn\mathbf{V}\,\mathbf{V}) + \nabla p - en\left(\mathbf{E} + \frac{1}{c}\mathbf{V} \times \mathbf{B}\right) = \mathbf{R} \ . \tag{6}$$

where m is the mass of a particle, c is the speed of light, p is pressure, $\mathbf{E}$ is the electric field and $\mathbf{B}$ is the magnetic field. $\mathbf{R}$ is the source of momentum, to be described in detail later. Note that both of these equations are in conservative form, and this is the way that they are numerically differenced in the code.

For conservation of energy, we start from the heat-balance equation, (Eq. (1.23) of Braginskii in reference 7)

$$\frac{3}{2}\frac{\partial nT}{\partial t} + \nabla \cdot \left(\frac{3}{2}nT\mathbf{V}\right) + nT\nabla \cdot \mathbf{V} + \Pi : \nabla\mathbf{V} + \nabla \cdot \mathbf{q} = Q \tag{7}$$

Here $\mathbf{q}$ is the heat flux and Π is the viscosity tensor. Q is the heat source term, to be described in detail later. Ignoring viscosity, this becomes

$$\frac{3}{2}\frac{\partial nT}{\partial t} + \nabla \cdot \left(\frac{3}{2}nT\mathbf{V}\right) + nT\nabla \cdot \mathbf{V} + \nabla \cdot \mathbf{q} = Q \tag{8}$$

The second term can be divided as follows:

$$T\nabla \cdot n\mathbf{V} + n\mathbf{V} \cdot \nabla T \ .$$

The first term above can be combined with the appropriate time derivative term of Eq. (8) to give the continuity equation scaled by T.

$$\frac{3}{2}T\left(\frac{\partial n}{\partial t} + \nabla \cdot nV\right) = \frac{3}{2}TS_p \tag{9}$$

Writing

$$Q^* = Q - \frac{3}{2}TS_p \ . \tag{10}$$

and dividing Eq. (8) by $(3/2)\,n$ leaves us

$$\frac{\partial T}{\partial t} + \mathbf{V} \cdot \nabla T + \frac{2}{3}T\nabla \cdot \mathbf{V} = \frac{2}{3n}(Q^* - \nabla \cdot q) \ . \tag{11}$$

The second and third terms can be rewritten as

$$\nabla \cdot (T\mathbf{V}) - \frac{1}{3}T\nabla \cdot \mathbf{V} \ . \tag{12}$$

This leads to the following equation for temperature:

$$\frac{\partial T}{\partial t} + \nabla \cdot (T\,\mathbf{V}) - \frac{1}{3}T\nabla \cdot \mathbf{V} = \frac{2}{3n}(Q^* - \nabla \cdot \mathbf{q}) \ . \tag{13}$$

Heat conduction is dominated by the electrons, and thus $\mathbf{q}$ is only present in the electron temperature equation, or, $\mathbf{q} = \mathbf{q_e}$. The form for $\mathbf{q_e}$ is:

$$\mathbf{q_e} = \kappa_\perp^e \nabla_\perp (kT_e) \ . \tag{14}$$

Here k is Boltzman's constant. $\kappa_\perp^e$ is the perpendicular electron thermal conductivity and is given as

$$\kappa_\perp^e = 4.7\frac{nkT_e}{m_e\omega_{ce}^2\tau_e} \ . \tag{15}$$

Here ω_{ce} is the electron gyrofrequency and τ_e is the basic collisional time.

To close the fluid equations, the equation of state for pressure is

$$p = nkT \ . \tag{15}$$

The Source Terms

The source terms are from various collision processes with the neutral gas, including atomic reactions. The details of the various source terms will now be presented.

The atomic reactions included here are ionization, charge-exchange and recombination and are characterized as follows.

Electron Impact Ionization:

$$e + H^o \rightarrow H^+ + 2e \ , \tag{17}$$

Resonant charge–exchange:

$$\overset{\text{hot}}{H^+} + \overset{\text{cold}}{H^o} \rightarrow \overset{\text{cold}}{H^+} + \overset{\text{hot}}{H^o} \ , \tag{18}$$

Collisional–radiative recombination:

$$e + H^+ \rightarrow H^* + h\nu \ , \tag{19}$$

and electron three–body recombination:

$$e + H^+ + e \rightarrow H + e \ . \tag{20}$$

In the recombination reactions above, the names describe the way the energy released by the recombination is carried away. H^* is an excited state, and $h\nu$ represents photons.

The particle source term, S_p, consists of sources from atomic reactions between the plasma and the neutral gas, which can be broken into three terms

$$S_p = S_{\text{ion}} + S_{\text{cx}} + S_{\text{rec}} \ . \tag{21}$$

Here S_{ion} is the source of particles from electron impact ionization, S_{cx} is the source of particles from resonant charge-exchange and S_{rec} is the source of particles from the recombination reactions.

The specific particle source terms have the following form:

$$S_{\rm rx} = n_1 n_2 \langle \sigma v \rangle_{\rm rx} \ . \tag{22}$$

n_1 and n_2 are determined by the species involved in the reaction. $\langle \sigma v \rangle_{\rm rx}$ is the reaction-rate for the specific reaction. The reaction-rates have been previously calculated and stored in a lookup table to be used by the code. The cross-section, σ, is temperature dependent. The average reaction-rates $\langle \sigma v \rangle$ was calculated assuming a Maxwellian velocity distribution for both species involved in the reaction.

The momentum source term has the same form as the particle source term. Specifically,

$$R = R_{\rm ion} + R_{\rm cx} + R_{\rm rec} \ . \tag{23}$$

The R's represent the source of momentum from the various atomic reactions,or:

$$R_{\rm rx} = (m\mathbf{V})_1 \, n_1 n_2 \langle \sigma v \rangle_{\rm rx} \ . \tag{24}$$

In addition, the **R** term contains elastic collisions between the plasma and neutrals, i.e., collisions that do not lead to atomic reactions. These elastic collisions are commonly referred to as friction. The frictional momentum transfer can be modeled as (for ions scattering off of neutrals)

$$R_{\rm f,in} = mn \left(V_n - V_i \right) \nu_{in} \ , \tag{25}$$

where ν_{in} is the collision frequency for scattering of ions by neutrals.

From momentum conservation we know that $R_{\rm f,in} = R_{\rm f,ni}$. Electrons also scatter elastically from the neutrals, but in the hybrid model, this is taken into account in the term for the plasma's resistivity (to be described later).

The last source term to consider is the source term for internal energy, Q. This includes the internal energy brought in via atomic reactions,

$$Q = Q_{\rm ion} + Q_{\rm cx} + Q_{\rm rec} \ . \tag{26}$$

Each Q has the form

$$Q_{rx} = \left(\frac{3}{2}nkT\right)_1 n_1 n_2 \langle \sigma v \rangle_{rx} \ . \tag{27}$$

For the ions there is an additional term for ion heating from the electrons

$$Q_i = \frac{3m_e}{m_i}\frac{nk}{\tau_e}\left(T_e - T_i\right) \ . \tag{28}$$

Electromagnetic Terms

All that is left is to find equations for **E** and **B**. In a hybrid plasma model, both come from the electron momentum equation.

In the limit of small electron inertia, the electron momentum equations reduced to

$$\mathbf{E} = -\frac{\nabla nkT_e}{en} - \frac{1}{c}\mathbf{u}_e \times \mathbf{B} + \eta \mathbf{J} \ , \tag{29}$$

where η is the plasma resistivity. The last term of this equation, $\eta\mathbf{J}$, is simply the **R** term in the notation used for the ion momentum equation. In other words, the friction of electrons scattering off of ions. As mentioned above, this term must also account for the scattering of electron off of neutrals. This is taken into account in the η term.

$$\eta_{total} = \eta_{en} + \eta_{ei} \ . \tag{30}$$

The electron momentum equation can be considered the Ohm's Law for the system. It should be emphasized that the velocity in the Lorentz term of this equation is the *electron* velocity, $\mathbf{u}_e$, not the fluid velocity **V**. These two velocities are related through the current,

$$\mathbf{J} = en\left(\mathbf{V} - \mathbf{u}_e\right) \ , \tag{31}$$

or,

$$\mathbf{u}_e = -\frac{1}{en}\mathbf{J} + \mathbf{V} \ . \tag{32}$$

Thus, the $\mathbf{u}_e \times \mathbf{B}$ term can be expanded to the form

$$\mathbf{V} \times \mathbf{B} - \frac{1}{en}\mathbf{J} \times \mathbf{B} \ . \tag{33}$$

This second term is commonly referred to as the Hall current term. In a more familiar form, the electron momentum equation becomes

$$\mathbf{E} + \mathbf{V} \times \mathbf{B} = \eta \mathbf{J} + \frac{1}{en} (\mathbf{J} \times \mathbf{B} - \nabla p_e) \ . \tag{34}$$

However, we will use Eq. (29) and Maxwell's equations to transform the electron momentum equation into an equation for $\mathbf{B}$.

The radiation-free limit of Ampere's law is

$$\nabla \times \mathbf{B} = \frac{4\pi}{c} \mathbf{J} \ . \tag{35}$$

Faraday's law is

$$\nabla \times \mathbf{E} = -\frac{1}{c} \frac{\partial \mathbf{B}}{\partial t} \ . \tag{36}$$

Introducing the magnetic vector potential ($\nabla \times \mathbf{A} = \mathbf{B}$) in the Coulomb gauge, and utilizing Maxwell's equations we can transform the electron momentum equation to

$$\dot{\mathbf{A}} = c \frac{\nabla p_e}{en} + \mathbf{u}_e \times \mathbf{B} - \frac{c^2}{4\pi} \eta (\nabla \times \mathbf{B}) \ . \tag{37}$$

The θ component of this equation will give us both B_r and B_z. Finally, if we take the curl of the electron momentum equation, and again utilizing Maxwell's equations, we obtain the equation which was used to advance B_θ numerically.

The electron velocity components are given via the relationship between the fluid velocity and current. Specifically,

$$\begin{aligned} u_{er} &= V_{ir} + \frac{c}{4\pi en} \frac{\partial B_\theta}{\partial z}, \\ u_{er} &= V_{ir} + \frac{c}{4\pi en} \nabla^2 \mathbf{A}|_\theta, \\ u_{ez} &= V_{iz} - \frac{c}{4\pi en} \frac{1}{r} \frac{\partial (r B_\theta)}{\partial r}. \end{aligned} \tag{38}$$

This completes the description of the equations for numerical modeling of the system.

Boundary Conditions

To complete the formulation of the problem one must specify consistent boundary conditions (BC's) for the equations discussed above. The geometry is a cylindrically symmetric duct. BC's must be specified at the inflow, z_{min}, outflow, z_{max}, $r = 0$, and the wall, r_{max}.

The inflow is assumed completely specified for the plasma and held fixed in time. The same is assumed for the neutral gas for axial injection. If radial injection is used, z_{min} becomes an *outflow* boundary for neutrals, also to be described later.

At the origin, $r = 0$, all quantities are assumed symmetric in θ which leads to the BC $\partial/\partial r = 0$. This holds for all quantities except A_θ. The BC for A_θ is Dirichlet zero. L'Hôpital's rule is utilized to ensure the fields derived from the vector potential is appropriate.

At the wall, r_{max}, A_θ is specified. For the fluid quantities, most are set as Neumann zero. The exception is temperature. In some cases the temperature is specified.

The most difficult BC's occur at z_{max}. Conventional *outflow* boundary conditions are used for the neutral gas, e. g., simple interpolation back in z. When the same BC's are attempted for the plasma, the computation failed eventually due to the problem that the plasma fluid reflects (numerically) from the outflow boundary. Many different BC's were attempted for the plasma fluid at z_{max}. The best results were obtained by simply interpolating back up a flux surface (magnetic field line), and setting the fluid quantities constant along the field line just at z_{max}. In this sense the magnetic field line is approximating a characteristic, even though in actuality it is not. To date, the best results have been obtained using the above BC's for the system.

Discussion

Our problem is many degrees more general than a simple one fluid MHD problem and is therefore many degrees more complex. Instead of solving one set of fluid equations, we are solving three sets of fluid equations – one set for ions and one set for electrons plus the neutral transport equation. Instead of steady state we are solving the time dependent problem. The reactions between species were taken into account. The coordinate system is cylindrical instead of a two dimensional Cartesian. The electron stream and the ion stream are governed by different time scales. The plasma time scale is many orders of magnitude faster than the neutral jet.

We were facing the difficulty of energy and particle conservation, numerical instability and boundary problems, particularly the outflow boundary. If not properly treated the plasma fluid will reflect numerically from the outflow boundary as discussed earlier. A normal characteristic solution method using CDF failed because of a diverging magnetic field. The problem was finally resolved by using a combination of ghost cells and a characteristic like solution based on magnetic field lines.

The size of the code is very large and computation time is very long. At present we are carrying out a quick scan over a wide range of parameter space to survey the effect. Some cases will be selected for a focused study later. The geometry of the tandem mirror device is shown schematically in Fig. 5a. The expanded exhaust section is shown in Fig. 5b and is marked by the coordinate axis $r-z$, where $r=0$ is the centerline of the device. $Z=0$ is the entrance of the plasma into the exhaust. Figure 6 is the density contour of plasma and neutral with a coaxial injection of gas jet. The boundary layer was formed which reconfirms our early steady state solution. Figure 6a is the flow of plasma without neutrals at 4μs. The plasma is seen fanned out along the field lines. Figures 6b through 6d show that plasma with coaxial neuteral jet at 2μ, 3μ and 4μ respectively. The plasma was contained and boundary layer was formed. However, the neutral jet was eroded downstream. Figure 7 shows density contour of plasma and neutrals when the neutral was injected radially. The plasma was contained better but neutrals were eroded at the tip. Figure 8 shows the coaxial injection at increasing neutral density. It shows that the plasma was contained to a

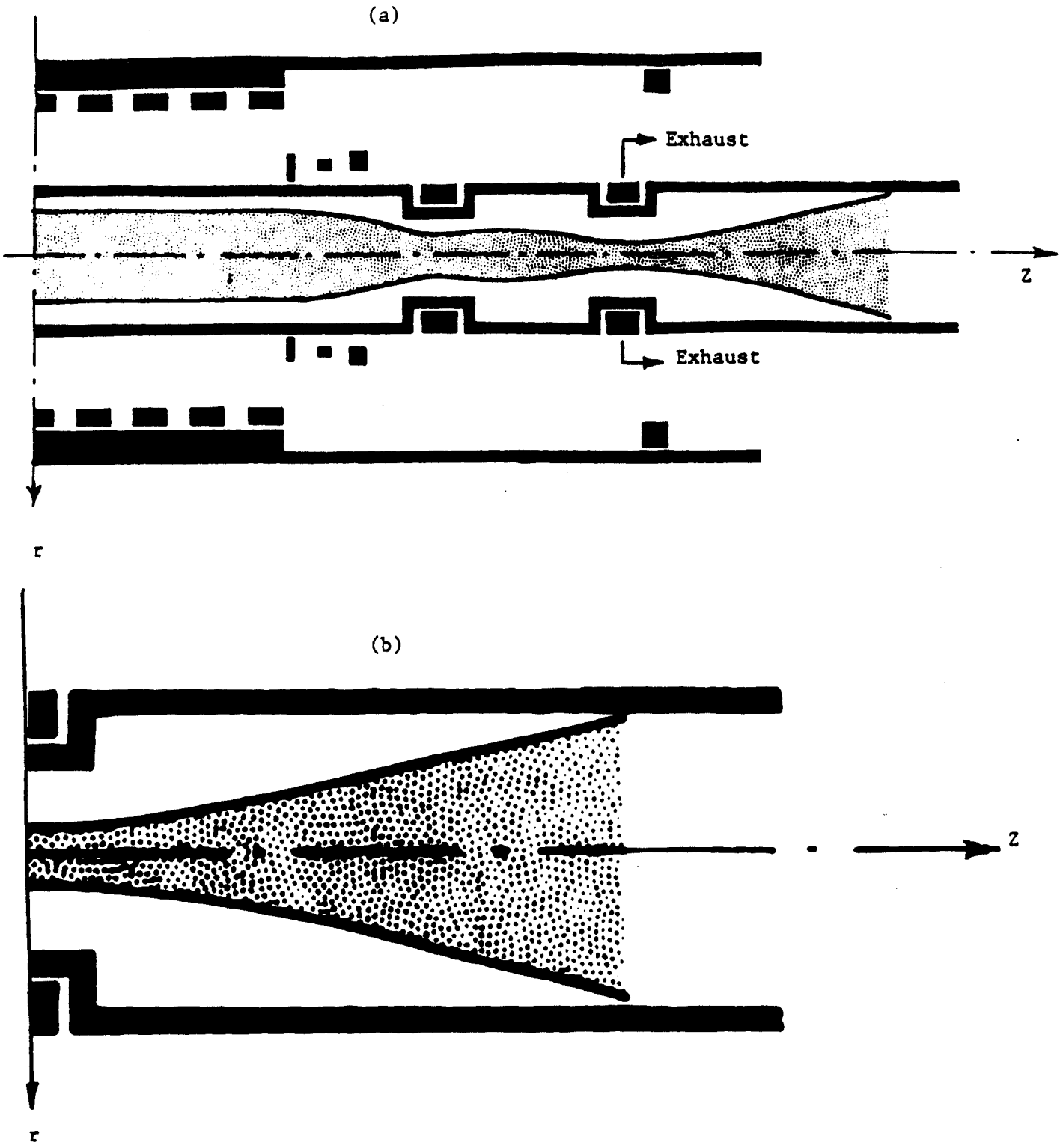

Figure 5. Schematic picture of the Tandem Mirror Plasma Rocket: (a) Side view of the device with exhaust duct where the shaded area represents plasma; (b) The expanded exhaust duct.

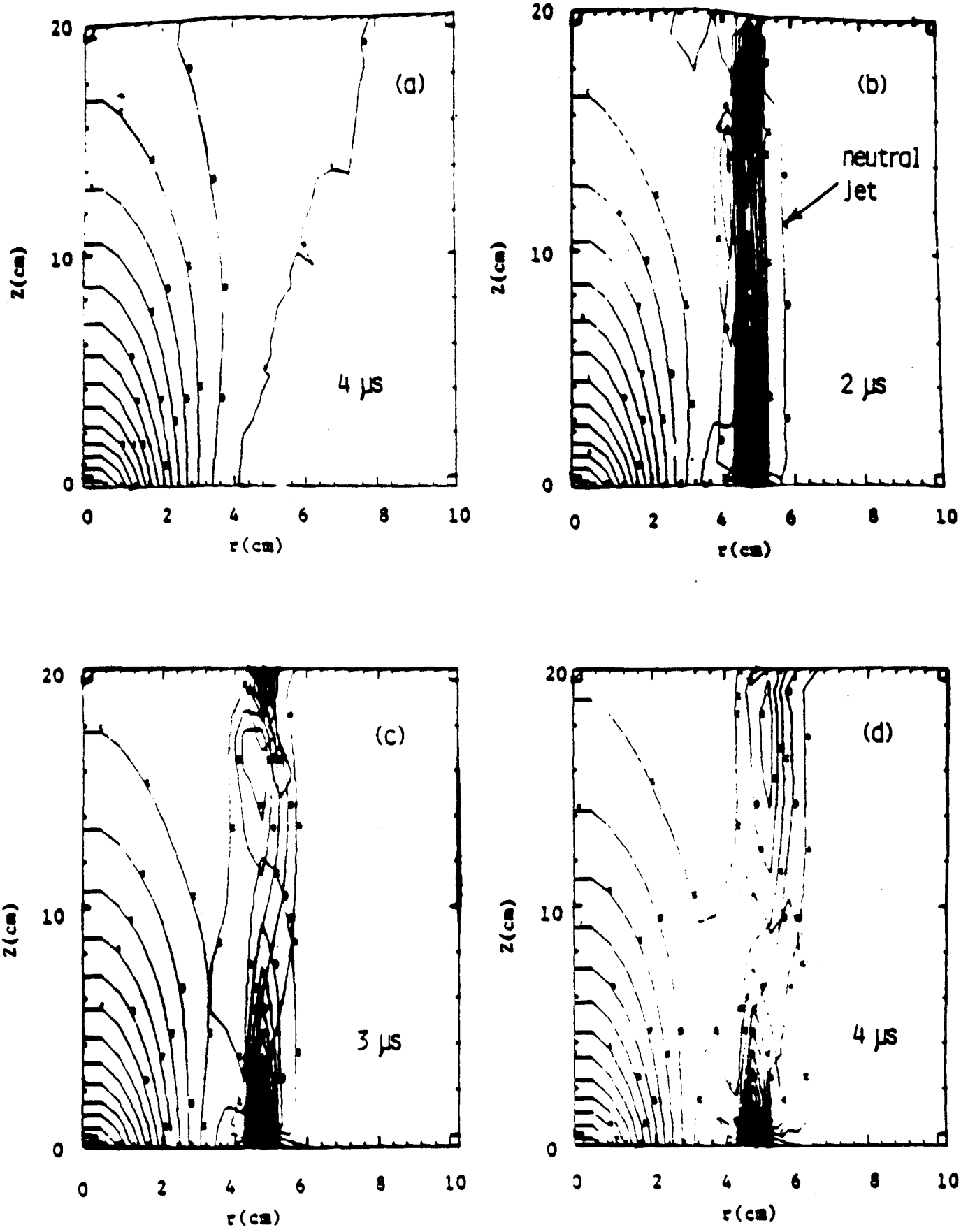

Figure 6. Plasma Neutral interaction in the exhaust,(a) Plasma expands as the field lines without neutral injection, (b),(c), and (d) Boundary layer was formed with axial neutral injection. Neutral gas was gradually eroded at later time.

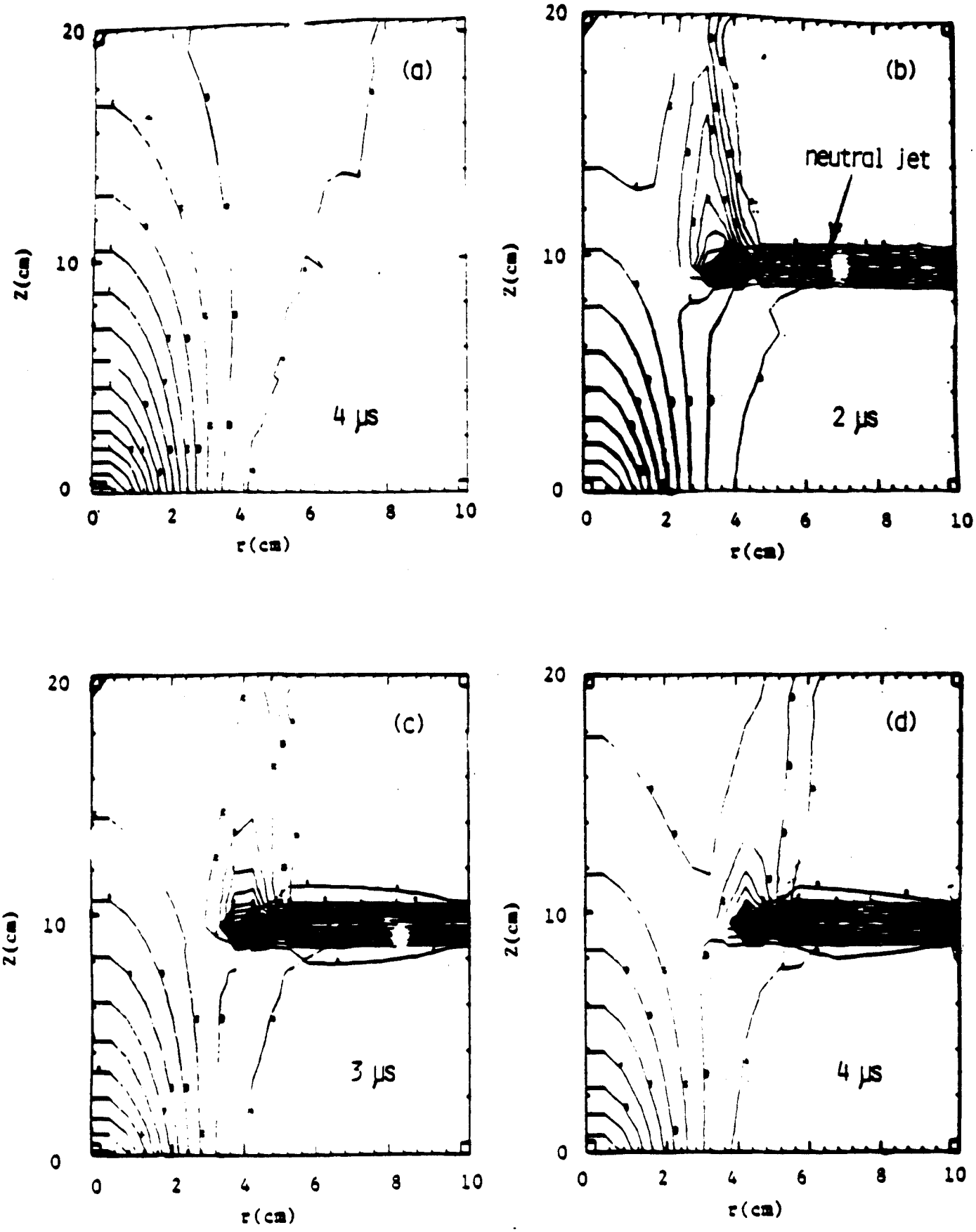

Figure 7. Plasma neutral interction in the exhaust, (a) Plasma expands as the field line without neutral injection. (b),(c),and (d) boundary layer was formed when neutral was injected radially.

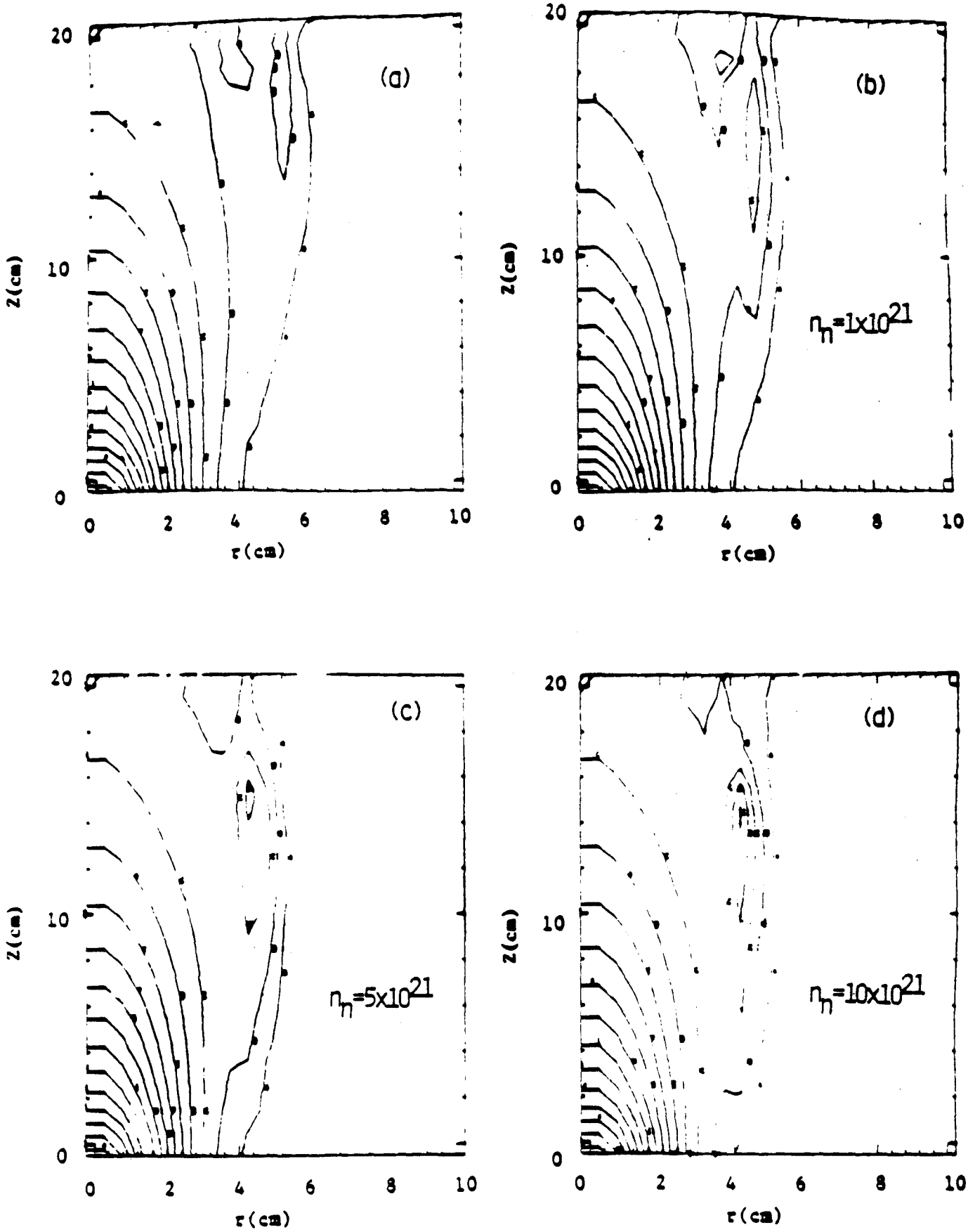

Figure 8. Plasma neutral interaction in the exhaust with increasing neutral density during axial injection. Plasma is more constricted at higher density

smaller radius at $n_n = 10 \times 10^{21}$ m^{-3} in Fig. 8d than at the lower density of $n_n = 1 \times 10^{21}$ m^{-3} in Fig. 8b.

In the radial injection case the flow characteristics was further improved by increasing the width of the radial gas jet. The flow time has been extended to 23μ which is nearly steady state. The contour plots at 2, 3 and 4μs are shown in Fig. 9.

Figures 10 (a1) and 10 (a2) show the average radial and axial ion temperature profiles of the plasma without injection. Figures 10 (b1) and 10 (b2) are the profiles for the plasma with axial injection. Figures 10 (c1) and 10 (c2) are the profiles with radial injection.

Figure 10 (a1) shows that the tail of the temperature profile extends to 7.7 cm. Figure 10 (b1) shows that tail was pushed back to 5.5 cm by the boundary layer created with a neutral jet. The ion temperature was nearly the same, therefore it was not deteriorated by the gas except at the edge where the temperature was reduced as expected. There was almost no change in axial profile. These effects can be seen from the superposition of the two radial profiles and axial profiles shown in Fig. 11 (a1) and 11 (a2).

The change in radial and axial profiles for the plasma with radial injection of wider width was significant. The superposition of these profiles with the profiles for no injection is shown in Figs. 11 (b1) and 11 (b2). Radially the temperature reduced further at the boundary but increased in the center core. Furthermore, the core temperature is uniform to $r = 1.7$ cm and drops sharply to a low temperature at $r = 3.7$ cm. This unexpected characteristic will improve the propulsion efficiency which is unique to the system. The axial profile in Fig. 11 (b2) shows that the high temperature plasma flows forward.

The comparison of radial and axial density profiles without gas injection and with axial and radial gas injections are shown in Fig. 12. The changes are much more appreciable than temperature profiles. The density at the edge for axial injection increased as shown by Fig. 12 (b1) where the temperature decreased as shown in Fig. 11 (b1). Again there is no noticable change in the axial profile. For radial injection the density increased drastically both at the edge and in the downstream axial direction as shown in Figs. 12 (c1) and (c2), respectively. The density increases were about eight times larger than in the axial injection. Because of a large difference in scale, presently these figures cannot be superimposed.

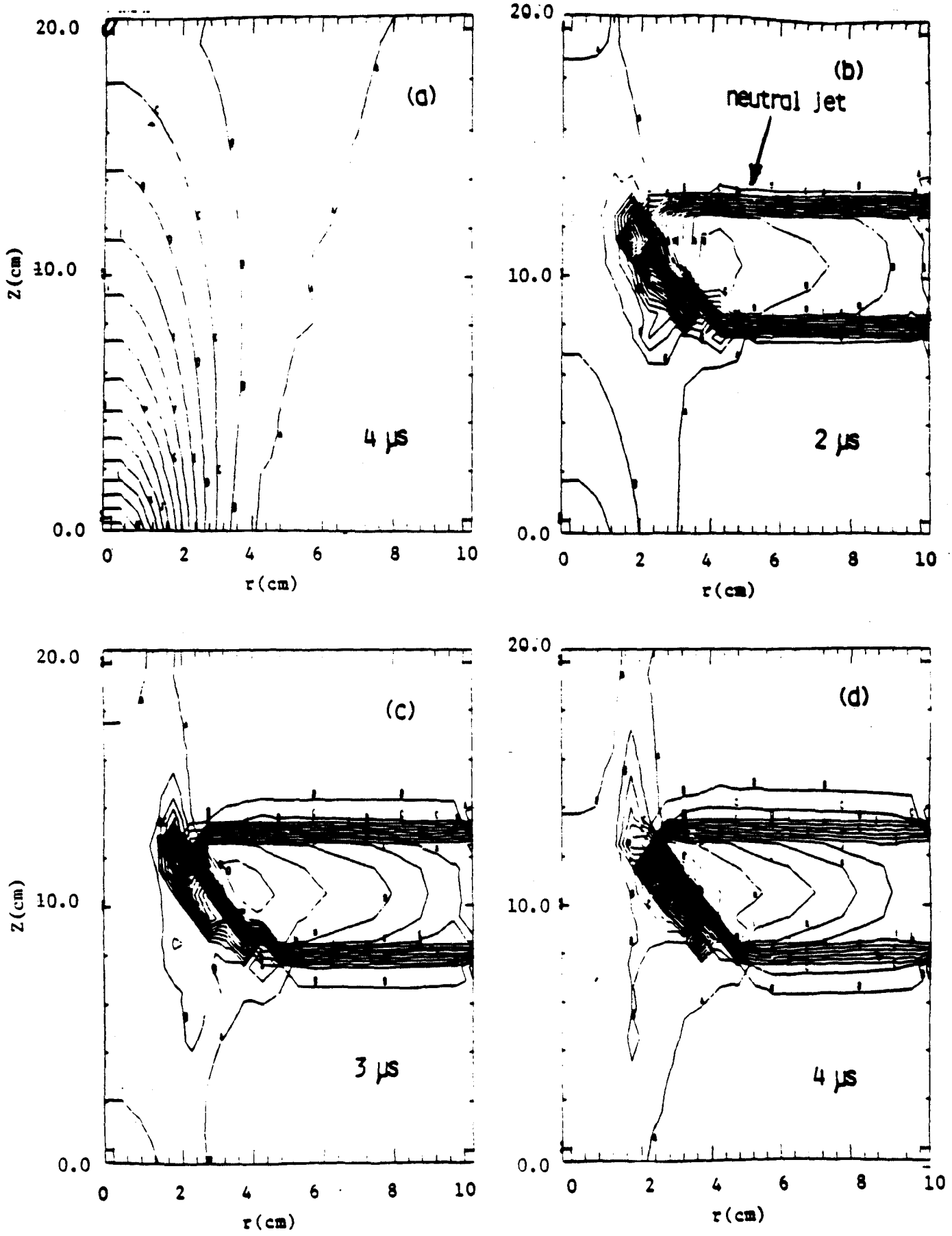

Figure 9. Plasma-gas interaction with wider radial gas injection as compared with that described in figure 7.

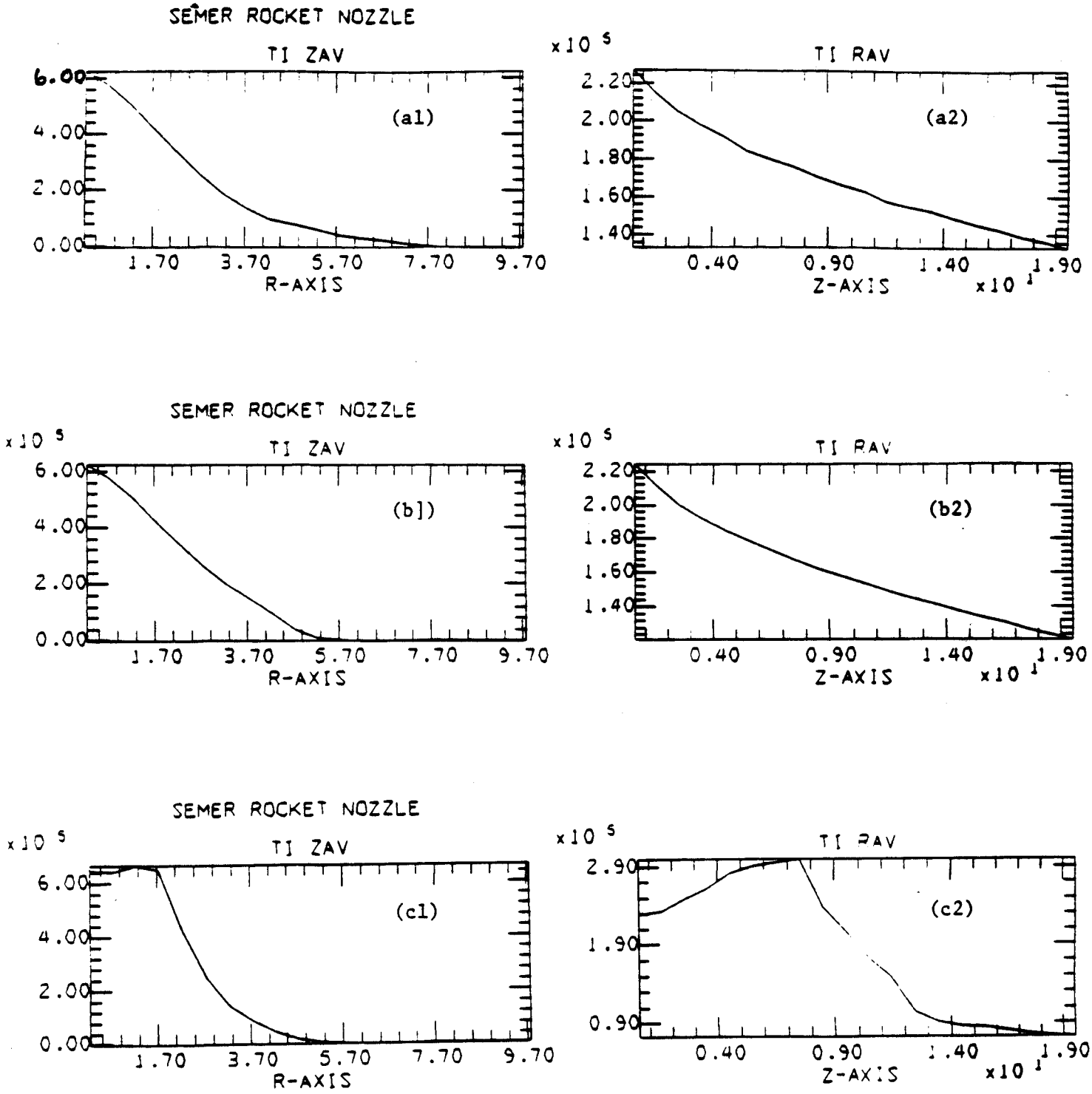

Figure 10. Averaged radial and axial ion temperature profiles : (a1) and(a2) without injection; (b1) and (b2) with axial injection: (c1) and (c2) with radial injection

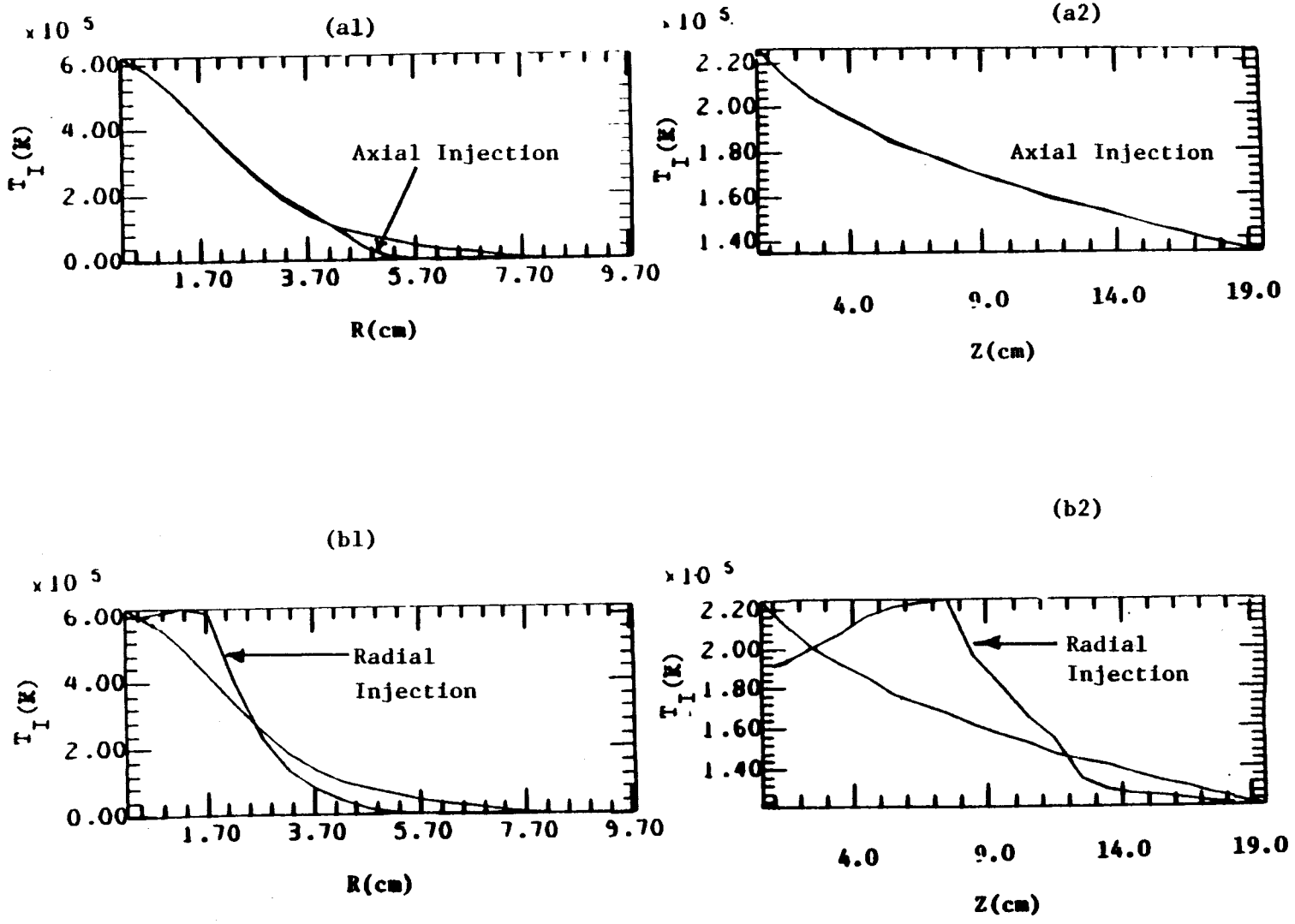

Figure 11. Comparison of temperature profiles without gas injection with the the profiles with axial gas injection (a1) and (a2), and with radial gas injection (b1) and (b2).

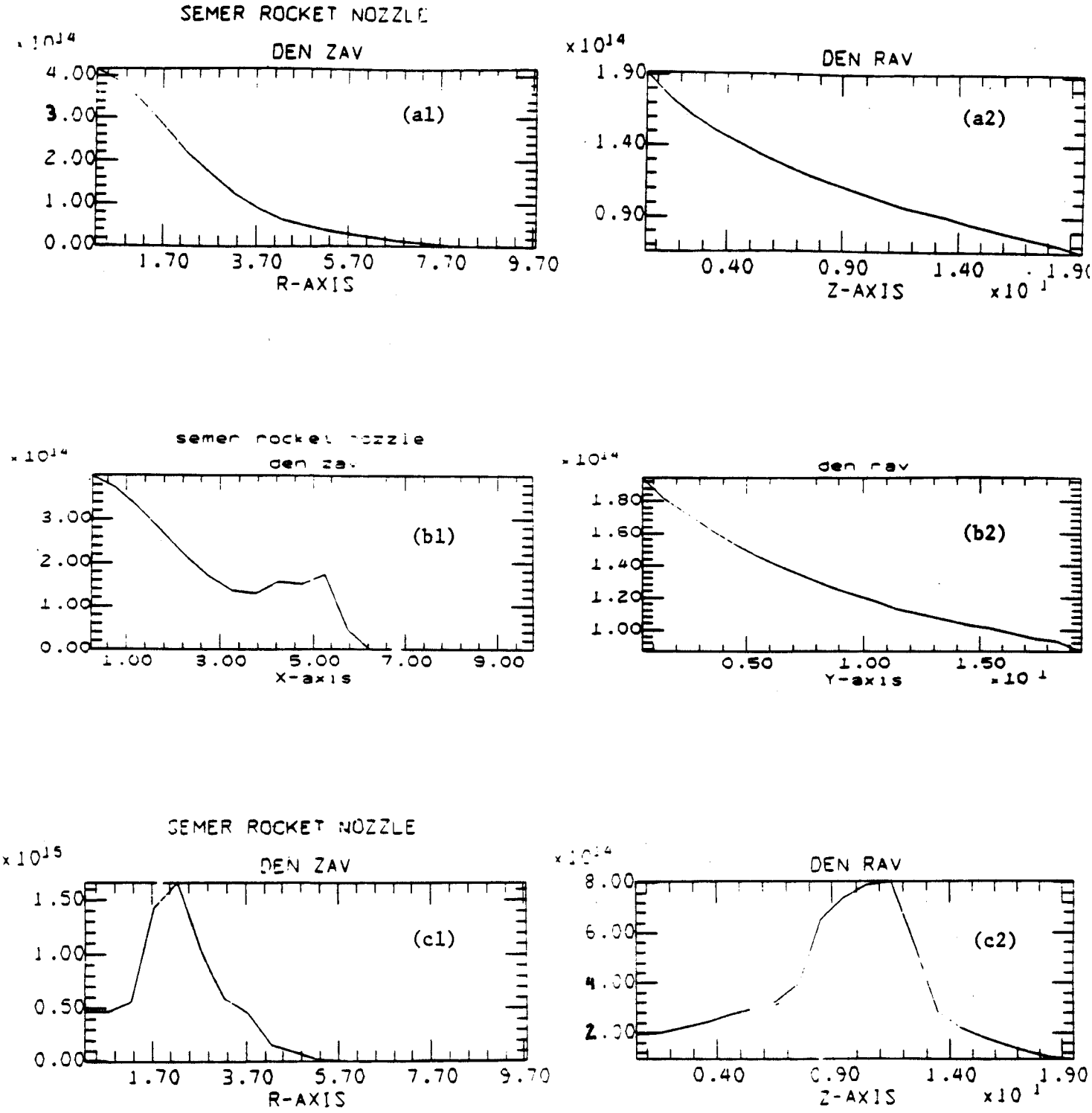

Figure 12. Averaged radial and axial ion density profiles: (a1) and (a2) without injection; (b1) and (b2) with axial injection; (c1) and (c2) with radial injection

These analyses show that injection angle, gas flow rate and density are very important and need to be studied thoroughly. There is a wide range of parameter space that has to be covered in order to understand the dynamic properties of this plasma-gas system.

This code can be modified for MPD and arcjet studies. The theory described is fundamental for any plasma propulsion. Currently the theory used in the code developed for MPD and arcjet is the reduced one-fluid MHD formulation. In reality all these systems should consist of at least three fluids as discussed here.

In any plasma device the electron and ion temperature are different. Particularly, in a device like MPD or Arcjet, where the plasma is produced through electrical discharge, the gas may not be fully ionized and there will be large amounts of neutral gas. The degree of ionization and the interaction between the species (eletron, ion and neutral) should be important. The electrons have very high mobility and determine the current flow. In principle the thrust of these devices is from the $\vec{j} \times \vec{B}$ force. Therefore it is to the best advantage of these system that the plasma behaves as a single fluid. Otherwise the thrust will be determined by the temperature of the ions which are the momentum carrying species. Therefore the detailed study of the microscopic properties of the plasma using the time dependent and multi-species transport code may allow us to learn the details of the current flow, magnetic field and energy distribution and the density of the species involved. This may lead us to learn conditions for single fluid operation.

Because there is no internal electrode in the exhaust of the hybrid plume system, there is no internal boundary. The initial conditions of the plasma injected from the tandem mirror device are known. To adapt this code for MPD and Arcjet studies, the boundary conditions at the internal electrodes and the initial conditions have to be worked out. Our experience is that to incorporate the time dependent internal boundary conditions is not trivial. To assure correct physics and numerical stability requires a considerable amount of effort.

2.4 ICRH Plasma Heating

Present fusion devices use ICRF power and neutral beams to heat the plasma. Since the neutral beam is larger and much more complex than ICRF, we chose to use the ICRF heating method.

The modeling of ICRH heating of plasma has been done and reported in the past which provided the guideline for antenna design. Analytical studies on slab models was also done. For the completeness of discussion they are reviewed here.

The analysis of the problem requires numerically solving for the fields in the vacuum and plasma regions. A code developed by B. McVey [8] was used to solve this problem for different antenna geometries. The theory used in this code is briefly summarized below.

Theory

The code analyzes Maxwell's equations

$$\nabla \times \vec{E} = -\frac{\partial \vec{B}}{\partial t} \tag{39}$$

$$\nabla \times \vec{B} = \frac{1}{c^2}\frac{\partial \vec{E}}{\partial t} + \mu_0 \vec{J} \tag{40}$$

$$\nabla \cdot \vec{B} = 0 \tag{41}$$

$$\nabla \cdot \vec{E} = \frac{\rho}{\epsilon_0} \, . \tag{42}$$

The fields are Fourier-Laplace transformed

$$\frac{\partial}{\partial t} \rightarrow -i\omega \tag{43}$$

$$\frac{\partial}{\partial z} \rightarrow ik_z \tag{44}$$

and solved in both the vacuum and plasma regions. The difference between the vacuum and plasma region comes in the current term J.

$$\vec{J}_{vacuum} = 0 \tag{45}$$

$$\vec{J}_{plasma} = -i\epsilon_0\omega(\underline{\underline{\epsilon}} - \underline{\underline{I}}) \tag{46}$$

where $\underline{\underline{\epsilon}}$ is the dielectric tensor.

The code solves these equations by breaking up the cylinder into several concentric cylindrical regions, solving for the fields in each region, then matching the boundary conditions to couple to the next region with its different parameters of density, temperature.

Strata Wave Matching Geometry

The transverse fields in each region can be expressed in terms of E_z and H_z, which are found to be

VACUUM

$$E_z = E_1 I_n(\nu r) + E_2 K_n(\nu r) \tag{47}$$

$$H_z = H_1 I_n(\nu r) + H_2 K_n(\nu r) \tag{48}$$

PLASMA

$$H_z(r) = H_{z1} J_n(k_{\perp 1} r) + y_2 E_{z2} J_n(k_{\perp 2} r) \tag{49}$$

$$E_z(r) = E_{z2} J_n(k_{\perp 2} r) + z_1 H_{z1} J_n(k_{\perp 1} r) \ . \tag{50}$$

From these fields, the time averaged power flow per cross-sectional area can be calculated by

$$P(w/m^2) = \frac{1}{2} Re[\vec{E}(\vec{r}) \times \vec{H}^*(\vec{r})] \cdot \hat{a}_r \ . \tag{51}$$

The inward power flow is then found by

$$P(r = r_0) = -\frac{r_0}{2} \sum_n \int_{-\infty}^{\infty} Re[E_\phi H_z^* - E_z H_\phi] dk_z \ . \tag{52}$$

The power absorbed by the plasma is determined by the plasma currents flowing in phase with the electric field:

$$p(w/m^3) = \frac{1}{2} Re(\vec{E} \cdot \vec{J}^*) \ . \tag{53}$$

From the circuit point of view, the power transferred out of the antenna region is

$$P_c = -\frac{1}{2}\int \vec{E}\cdot\vec{J}^* d\vec{v} \tag{54}$$

$$P_c(w) = -\frac{1}{2}\sum_n \int_{-\infty}^{\infty} dk_z \int_b^d r(\vec{E}\cdot\vec{J}^*)\ . \tag{55}$$

The impedence is then found by

$$Z = \frac{2P_c(w)}{|I|^2} \tag{56}$$

Numerical Results

Seven types of antennae have been studied using the ANTENA computer code [8] and are shown in Fig. 13. Typical computed power absorption profiles by ions and electrons are shown in Fig. 14. The results are summarized in Table 1. The total input power used in these calculations is 100 kW.

The current in the coils necessary to provide 100 kW input power varies from about 2.5 to 8.5 kA. All coils are assumed to have circular cross sections with a radius of 1.0 cm located 4 cm radially from the plasma boundary. A reasonable limit for the current density is about 2 kA/cm^2, which is exceeded in the full turn, the line current, and the half Nagoya coils.

Table 1

Absorption for Various Antennae

Coil	I(kA)	J(kA/cm^2)	P_t(kW)	F_i(%)	F_e(%)	Efficiency(%)
Full turn	7.204	2.293	45.97	84.53	15.48	45.97
Saddle coil	3.342	1.064	49.23	97.85	2.15	49.23
Nagoya III	3.526	1.122	49.04	98.50	1.50	49.04
Aperture	2.738	0.872	28.72	98.48	1.52	28.72
Line current	6.735	2.144	54.05	96.04	3.96	54.05
Half loop	5.197	1.654	54.90	95.72	4.28	54.90
Half Nagoya	8.276	2.634	47.73	54.14	45.86	47.73

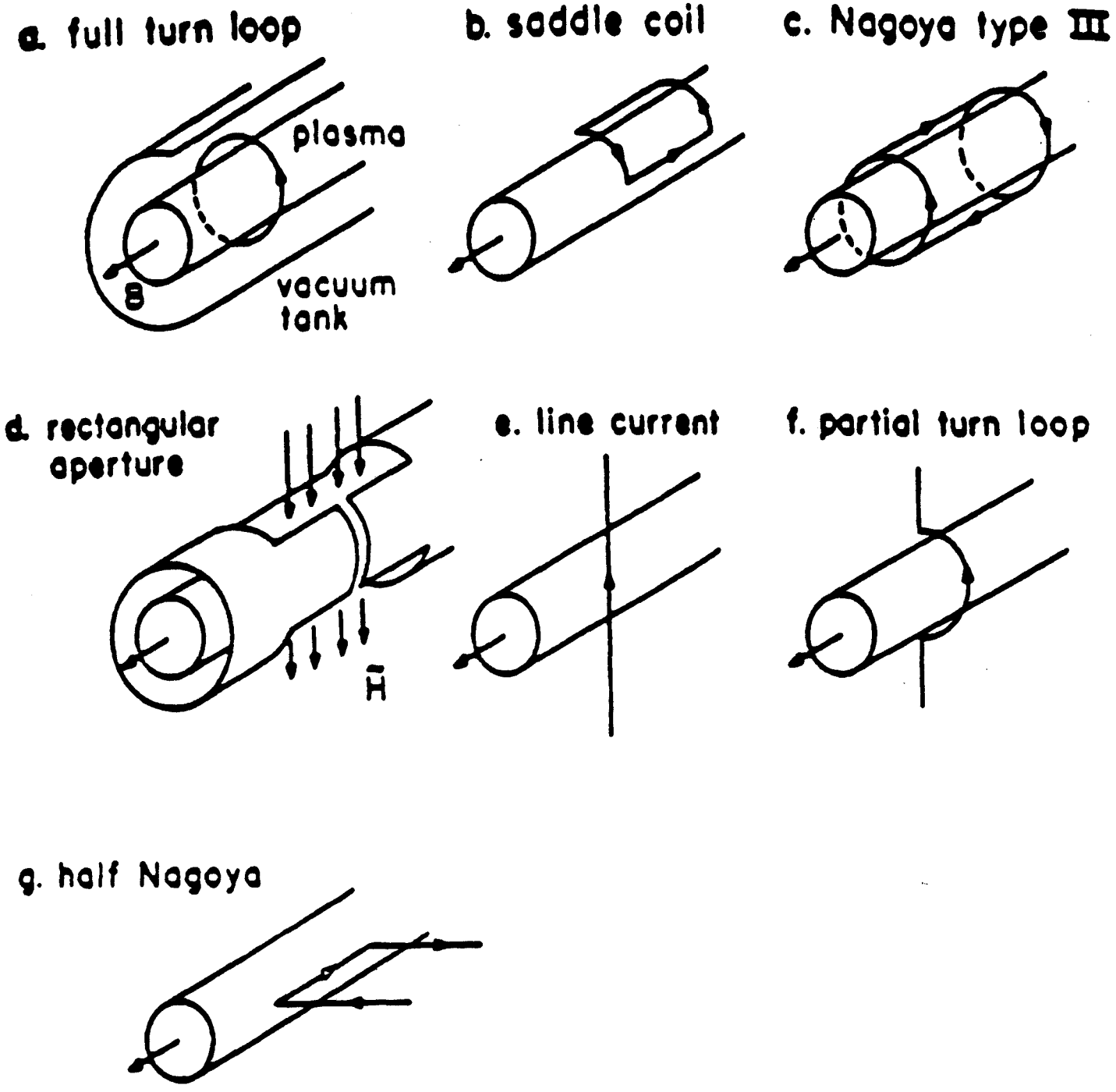

Figure 13. Various ICRF antennae studied.

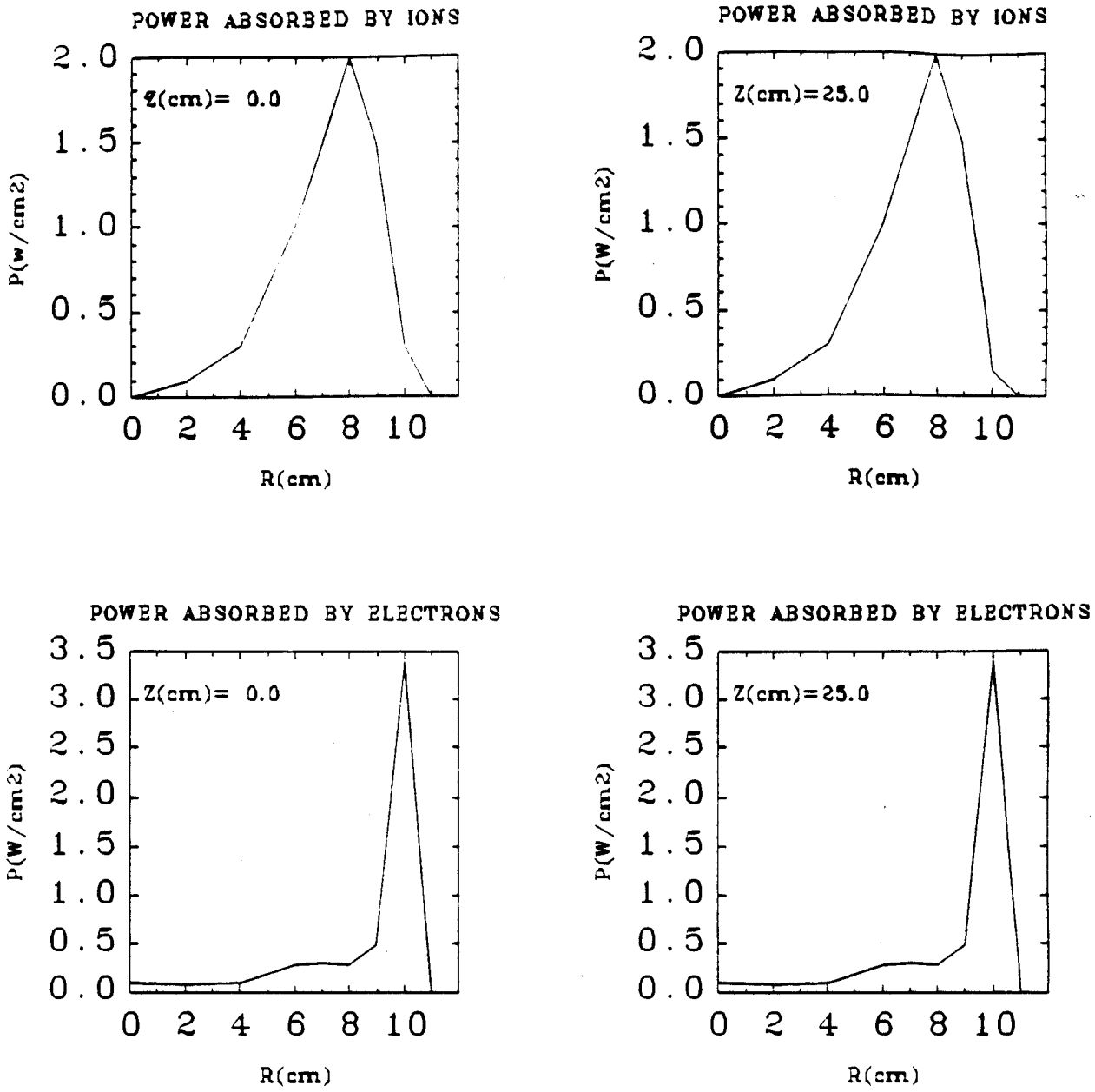

Figure 14. Typical absorption profiles.

I = coil current
J = coil current density
P_t = total power absorbed by ions
F_i = fraction of total power absorbed by ions
F_e = fraction of total power absorbed by electrons
P_a = power calculated by the antenna code
Efficiency = fraction of power input to antenna absorbed by the plasma

The results show that the half loop antenna has the highest efficiency of all the antennae considered. The ions in the system absorb 96% of this power while the electrons receive the balance. This is a desirable result since energy transfer from the ions to the neutrals is more efficient than from the electrons to the neutrals.

These preliminary results agree well with experimental ones which show ICRF heating efficiencies greater than 55% [9]. The theory of ICRF is not well developed. It is a very complicated problem which is worked on by all the researchers in the fusion community. We are only a small effort toward the contribution to the understanding and the improvement of a heating mechanism. We will continue to apply the new development in the fusion community to this study.

Based on the relative efficiencies of the antennae shown by these results, we have chosen two half-circle coils to provide ICRF heating at the initial stage. A full turn loop was not chosen because it seems to require a higher current and higher current density to provide the same input power. Two half loops will be used to maintain the symmetry of the plasma; a single partial loop tends to increase the plasma current on the antenna side. The half turn also has the advantage for our application of being light in mass compared to some of the other coils.

2.5 Analytical Modeling of ICRH Plasma Heating

The numerical model presented in the previous section is lacking physical insight. The analytical model based on a slab geometry was done in order to obtain the explicit dependence of heating on the antenna geometry. The power coupled from an antenna into

a plasma may be calculated if both the input antenna current and the loading resistance of the plasma are known. The power coupled into a plasma is calculated by

$$P = \frac{1}{2} R_p |I|^2 \tag{57}$$

where R_p is the plasma loading resistance, I the applied antenna current. Thus it is necessary to calculate a load resistance for the configuration desired. Although the physical geometry of the plasma rocket is cylindrical, the calculations are performed using a slab geometry to produce a resulting R_p that can be intuitively understood. The geometry is seen in Fig. 15. The results presented are obtained from Shepard [10].

The analysis is as follows. The antenna–plasma coupling region is separated into three regions: Region I is the vacuum between the chamber wall and the antenna, Region II is the vacuum between the antenna and the Faraday Shield, and Region III is the plasma region. The density profile in Region III is assumed to be a constant sloped line. The fields are solved in each of the three regions and then boundary conditions are used to couple the fields together. Complete knowledge of the fields then can be used to find the power coupled into the plasma by

$$P_A = -\frac{1}{2} \int_{-\infty}^{\infty} E_y|_{ant} J^*(n_z) \frac{dn_z}{2\pi} = \frac{1}{2} I^2 Z_A \tag{58}$$

where $E_y|_{ant}$ is the Electric field at the antenna surface, $J^*(n_z)$ the n_z-transformed antenna sheet current, and Z_A the Specific Radiation Impedence of the plasma. ($R_p = \mathrm{Re}(Z_A)$) Thus R_p can be found from the fields and a parametric dependence of the plasma loading dependence can be obtained.

The fields in Regions I and II are found by solving Maxwell's equations in free space.

$$\nabla \times \mathbf{E} = -\frac{\partial \mathbf{B}}{\partial t} \tag{59}$$

$$\nabla \times \mathbf{B} = \frac{1}{c^2} \frac{\partial \mathbf{E}}{\partial t} + \mu_0 \mathbf{J} \tag{60}$$

REGION I.

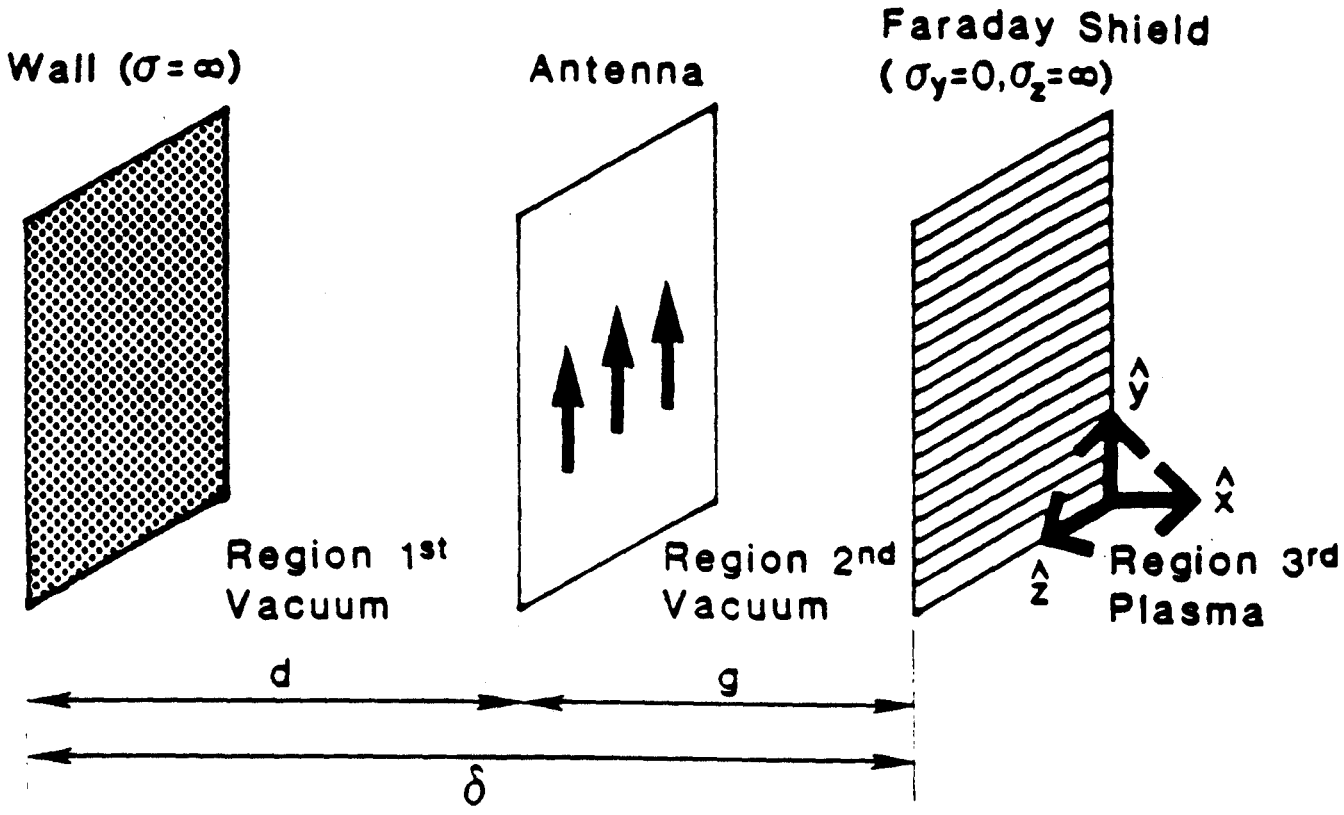

Figure 15. Geometry of the wall, antenna and shield in slab.

Defining c to be 1 (where c is the speed of light), the vacuum fields are found to consist of a linear combination of Transverse–Electric (TE) and Transverse–Magnetic (TM) modes:

$$\mathbf{E} = A_1\mathbf{E}_{TM} + A_2\mathbf{E}_{TE} \tag{61}$$

$$\mathbf{B} = A_1\mathbf{B}_{TM} + A_2\mathbf{B}_{TE} \tag{62}$$

Defining $n_x \equiv \sqrt{1 - n_y^2 - n_z^2}$, the following fields are obtained for Region I:

TM MODES:

$$\begin{aligned} E_x &= i(n_y^2 + n_z^2)\cos(n_x\zeta) \\ E_y &= n_x n_y \sin(n_x\xi) \\ E_z &= n_x n_z \sin(n_x\xi) \\ B_x &= 0 \\ B_y &= i n_z \cos(n_x\xi) \\ B_z &= -i n_y \cos(n_x\xi) \end{aligned} \tag{63}$$

TE MODES:

$$\begin{aligned} E_x &= 0 \\ E_y &= -n_z \sin(n_x\xi) \\ E_z &= n_y \sin(n_x\xi) \\ B_x &= (n_y^2 + n_z^2)\sin(n_x\xi) \\ B_y &= i n_x n_y \cos(n_x\xi) \\ B_z &= i n_x n_z \cos(n_x\xi) \end{aligned} \tag{64}$$

REGION II.

The difference between regions I and II is the jump in the B-Field across the antenna due to the surface current $J(n_y, n_z)$. Using the boundary condition $E_z(0) = 0$, one of the two constants A_2 can be found in terms of the other and the resulting field at the Faraday shield is :

$$
\begin{aligned}
Ex(0) &= iA_1 n_y (n_y^2 + n_z^2)\cos(n_x\delta) \\
E_y(0) &= A_1 n_x (n_y^2 + n_z^2)\sin(n_x\delta) \\
E_z(0) &= 0 \\
B_x(0) &= -A_1 n_x n_z (n_y^2 + n_z^2)\sin(n_x\delta) \\
B_y(0) &= iA_1 n_y n_z (n_y^2 + n_z^2)\cos(n_x\delta) \\
B_z(0) &= -iA_1 (n_y^2 + n_x^2 n_z^2)\cos(n_x\delta) - J(n_y, n_z)
\end{aligned}
\tag{65}
$$

REGION III.

The method of solution presented are from Lam et al.[11]. The fields in the plasma can be found by solving Maxwell's equations with the plasma contribution appearing in the current J. After Fourier–Laplace transforming and ignoring the initial condition, Maxwell's equations are reduced to :

$$
\begin{aligned}
\nabla \times \mathbf{E} &= i\omega \mathbf{B} \\
\nabla \times \mathbf{B} &= -i\omega \overline{\overline{\mathbf{K}}} \cdot \mathbf{E}
\end{aligned}
\tag{66}
$$

where $\overline{\overline{\mathbf{K}}}$ is the cold plasma dielectric tensor:

$$
\overline{\overline{\mathbf{K}}} = \begin{pmatrix} K_\perp & -iK_x & 0 \\ iK_x & K_\perp & 0 \\ 0 & 0 & K_\parallel \end{pmatrix}
\tag{67}
$$

where

$$
\begin{aligned}
K_\perp &= 1 - \sum_\alpha \frac{\omega_{p\alpha}^2}{\omega^2 - \Omega_\alpha^2} \\
K_x &= \sum_\alpha \frac{\omega \omega_{p\alpha}^2}{\Omega_\alpha (\omega^2 - \Omega_\alpha^2} \\
K_\parallel &= 1 - \sum_\alpha \frac{\omega_{p\alpha}^2}{\omega^2}
\end{aligned}
\tag{68}
$$

where α is the species index.

Expanding $K_{\|}$, it is seen that the dielectric tensor $\overline{\overline{\mathbf{K}}}$ can be separated into two terms, one of order $O(1)$ and another of order $O(1/\epsilon)$. (Where $\epsilon = m_e/m_i$) Maxwell's equations now become

$$\begin{aligned} \nabla \times \mathbf{E} &= i\omega \mathbf{B} \\ \epsilon \nabla \times \mathbf{B} &= i\overline{\overline{\mathbf{S}_*}} \cdot \mathbf{E} \end{aligned} \tag{69}$$

where

$$\overline{\overline{\mathbf{S}_*}} = \epsilon \overline{\overline{\mathbf{S}}} + S_0 \hat{z}\hat{z} \tag{70}$$

$$\begin{aligned} S_0 &= \frac{\omega_{pi}^2}{\omega^2} \\ \overline{\overline{\mathbf{S}}} &= \begin{pmatrix} S_\perp & iS_x & 0 \\ -iS_x & S_\perp & 0 \\ 0 & 0 & S_{\|} \end{pmatrix} \end{aligned} \tag{71}$$

$$\begin{aligned} S_\perp &= \frac{\omega_{pi}^2}{\omega^2 - \omega_{ci}^2} - 1 + \dots \\ S_{\|} &= \frac{\omega_{pi}^2}{\omega^2} - 1 \\ S_X &= \frac{\omega \omega_{pi}^2}{\omega^2 - \omega_{ci}^2} \end{aligned} \tag{72}$$

Expanding the Electric and Magnetic fields in orders of ϵ,

$$\mathbf{E} = \mathbf{E_0} + \epsilon \mathbf{E_1} + \cdots, \quad \mathbf{B} = \mathbf{B_0} + \epsilon \mathbf{B_1} + \cdots \tag{73}$$

it can be shown that Maxwell equations reduce to :

$$\begin{aligned} \frac{dE_y}{d\xi} - \left(\frac{n_y S_X}{S_\perp + n_z^2} \right) E_y &= i \left(1 + \frac{n_y^2}{S_\perp + n_z^2} \right) B_z \\ \frac{dB_z}{d\xi} + \left(\frac{n_y S_X}{S_\perp + n_z^2} \right) B_z &= i \left(\frac{S_X^2}{S_\perp + n_z^2} - S_\perp - n_z^2 \right) E_y \end{aligned} \tag{74}$$

The problem can be further reduced by examining the case of no propagation in the y-direction. In this case, Maxwell's equations are further reduced to

$$\frac{d^2E_y}{d\xi^2} + f(\xi)E_y = 0 \tag{75}$$

where

$$f(\xi) = \frac{S_X^2}{S_\perp + n_z^2} - S_\perp - n_z^2 \tag{76}$$

Approximating the function $f(\xi)$ by :

$$f(\xi) = \gamma(\xi) - (n_z^2 - 1) \tag{77}$$

where $\gamma(\xi)$ is the density profile.

The solution of the above differential equation is the Airy function:

$$E_y(\xi) = A_3\mathrm{Ai}(-\nu) - A_4\mathrm{Bi}(-\nu) \tag{78}$$

where

$$\begin{aligned} \nu &= \frac{M\xi - (n_z^2 - 1)}{M^{2/3}} \\ M &= \frac{n_0 m_i}{\epsilon B^2} \\ n_0 &= n(\xi = 1) \end{aligned} \tag{79}$$

Using the Outgoing Wave Boundary Condition by taking $\xi \to \infty$, it is seen that an outgoing wave has the wave property of $\mathrm{e}^{i(kx-\omega t)} = \mathrm{e}^{-i\omega t}\mathrm{e}^{ikx}$. Using the trigonometric identity

$$\mathrm{e}^{ikx} = \cos(kx) + i\sin(kx) \tag{80}$$

Asymptotically,

$$\begin{aligned} \mathrm{Ai}(-\nu) &\sim \frac{\sin(\frac{2}{3}\nu^{3/2} + \frac{\pi}{4})}{\nu^{1/4}\sqrt{\pi}} \\ \mathrm{Bi}(-\nu) &\sim \frac{\cos(\frac{2}{3}\nu^{3/2} + \frac{\pi}{4})}{\nu^{1/4}\sqrt{\pi}} \end{aligned} \tag{81}$$

Thus

$$E_y = A_3[i\mathrm{Ai}(-\nu) + \mathrm{Bi}(-\nu)] \tag{82}$$

Using Taylor Series Expansion [2] for small ν, the Electric and Magnetic fields are seen to be :

$$\begin{aligned} E_y(0) &= D[(i+\sqrt{3}) - (i-\sqrt{3})F(n_z^2-1)] \\ B_z(0) &= D(1-i\sqrt{3})FM \end{aligned} \tag{83}$$

where

$$F \equiv \frac{\Gamma(2/3)}{(3M)^{2/3}\Gamma(4/3)} \tag{84}$$

and

$$D \equiv \frac{A_3}{3^{2/3}\Gamma(2/3)} \tag{85}$$

Matching the vacuum and plasma fields at the Faraday Shield surface, the coefficients A_3 and A_1 can be found and the fields can be completely determined.

The solution is

$$E_y(0) = Jd\left[\frac{\sqrt{3}+i(4FM\delta-1)}{2FM\delta-1-i\sqrt{3}}\right] \tag{86}$$

The antenna sheet current transformed into the n_z space becomes

$$J(n_z) = I\frac{\sin(n_z\xi_0)}{n_z\xi_0} \tag{87}$$

where

$$\xi_0 = \frac{\omega w}{2} \tag{88}$$

The Specific Radiation Impedence (SRI) can then be found by integrating Eq.(2) and substituting into Eq.(1). The result is

$$Z_A = \frac{1}{2}\frac{d}{\xi_0}\left[\frac{\sqrt{3}+i(4FM\delta-1)}{1-i\sqrt{3}-2FM\delta}\right] \tag{89}$$

The loading resistance is then found to be

$$R_A = \frac{\sqrt{3}d}{\xi_0}\left[\frac{1-3FM\delta}{3+(1-2FM\delta)^2}\right] \tag{90}$$

From this relationship, the parametric dependence of the loading resistance can be seen. The results show that for increasing $FM\delta$, the loading resistance R_A decreases. The parametric results can be seen in Table 2. It is seen that to obtain the maximum loading resistance, the distance from the antenna to the wall, d, must be maximized but the distance from the wall to the Faraday shield, δ, must be minimized. It is also desirable to have a relatively low density plasma and a high magnetic field. The antenna width itself must also be kept as thin as possible to maximize the plasma loading resistance.

Table 2

Parametric Dependences of the Loading Resistance R_A

Variable	Significance of Variable	Result on R_A
d	d=Distance from Antenna to Wall	$d \uparrow$, $R_A \uparrow$
ξ	$\xi = W/2 \sim$ width of antenna	$\xi \uparrow$, $R_A \downarrow$
n_0	n_0 = density	$n_0 \uparrow$, $R_A \downarrow$
B	B = Magnetic field	$B \uparrow$, $R_A \uparrow$
δ	δ=Dist. from wall to Faraday Shield	$\delta \uparrow$, $R_A \downarrow$

Discussion

A 3-D cartesian analysis of the antenna geometry was carried out using the method of Shepard [10] and Lam [11]. The resulting plasma loading resistance shows a parametric dependence on d, ξ, n_0, B, and δ which are the distance from the antenna to wall, width of antenna, plasma density, magnetic field, and distance from the wall to the Faraday shield, respectively. It is seen that in order to maximize the plasma loading resistance, the antenna must be placed as close to the Faraday shield and as far away from the wall as possible. Other parametric dependences of the loading resistance indicates that a thinner antenna along with a lower density plasma and a higher magnetic field would yield a higher loading resistance.

Future work in this area would extend the treatment from a 3-D Cartesian geometry to a 3-D cylindrical geometry. This would better mock-up the IPPROC and perhaps yield a more accurate picture of the behavior of the loading resistance. Hot plasma effects will also be mocked up so as to better simulate the plasma inside the device.

3 Propulsion Projection

The exhaust velocity of the plasma injected from the mirror device is given by thermal velocity[12]

$$v = \sqrt{\frac{T}{Am}} \tag{91}$$

where T is the ion temperature in eV, m is the hydrogen ion mass in kG, and A is the mass number for heavy atoms. The velocity can be rewritten as

$$v = 0.979 \times 10^4 \sqrt{\frac{T}{A}} \ \text{m/s} . \tag{92}$$

Let us use 100 kW of power as a basis to find the range of feasible performance parameters. Given the power P in kW we obtain the mass flow rate

$$\dot{m} = \frac{2P}{v^2} = 2.090 \times 10^{-8} \frac{A}{T} P \ \text{mg/sec} \tag{93}$$

and the thrust

$$\text{Thrust} = \dot{m}v = 0.205 \sqrt{\frac{\text{A}}{\text{T}}} \text{P} \ \ \text{N} . \tag{94}$$

The exhaust cross-sectional area of this device is $S = 0.785 \times 10^{-2}$ m^2. One can obtain the required plasma density

$$n = \frac{\dot{m}}{SAmv} = 1.629 \times 10^{17} \sqrt{\frac{A}{T^3}} P \ \ \text{m}^{-3} . \tag{95}$$

The thrust and mass flow rate $\dot{m}$ are plotted as solid curves as a function of I_{sp} in Fig. 16, whereas the plasma temperature and density are plotted as dashed curves. The curves are self-explanatory. The thrust decreases from 100 N at $I_{sp} = 1,000$ sec to 0.6 N at $I_{sp} = 30,000$ sec. The plasma temperature T increases from 1 eV to 1 keV. The corresponding

density decreases from 1×10^{21} m^{-3} to 1×10^{17} m^{-3}. These plasma parameters are achievable in this device but harder toward low temperature and high density. This is where the hybrid plume comes in.

Figure 17 shows the power and mass flow rate as a function of I_{sp} (solid curves) at constant thrust of 20 N. Power increases from 100 kW to 2 MW and mass flow rate decreases from 2 mg/s to 0.7 mg/s for I_{sp} ranging from 1,000 sec to 30,000 sec. The temperature range is the same as in Fig. 17 for the same I_{sp} range. However, the density is two orders of magnitude lower.

Figure 18 shows the mass flow rate and power requirement as a function of thrust with constant I_{sp} of 3,000 sec. Therefore the temperature is fixed at 10 eV. The density is increased by two orders of magnitude than that in Figs. 16 and 17.

The present achieved conditions put us at the high I_{sp} (23,000) sec and low thrust 0.1 N. We are planning to work downward to increase thrust and reduce I_{sp}. These figures indicate the range of parameters we would like to achieve.

4 Physical Defficiency

The properties of the hybrid plume are governed by the physics of high temperature hydrogenic plasma interacting with hydrogen gas jets in a nonuniform magnetic field. The physics of such a system is not well known.

Theoretically the concept has been verified by a steady state fluid model in a uniform magnetic field with simplified assumptions. This was a step to demonstrate the principle of the hybrid plume. Dynamic flow characteristics have to be studied with a time dependent model in a nonuniform field. In a time dependent code proper treatment of the outflow boundary becomes very important. Now we have achieved this second step and we begin to understand the dynamic behavior of the plasma-neutral interaction. Since the parameter space is very large, a thorough study has to be carried out as the next step.

From the knowledge gained in this work we found a new defficiency in the theory. The pressure in the transport equation is assumed to be scalar. In both MPD and arcjet and

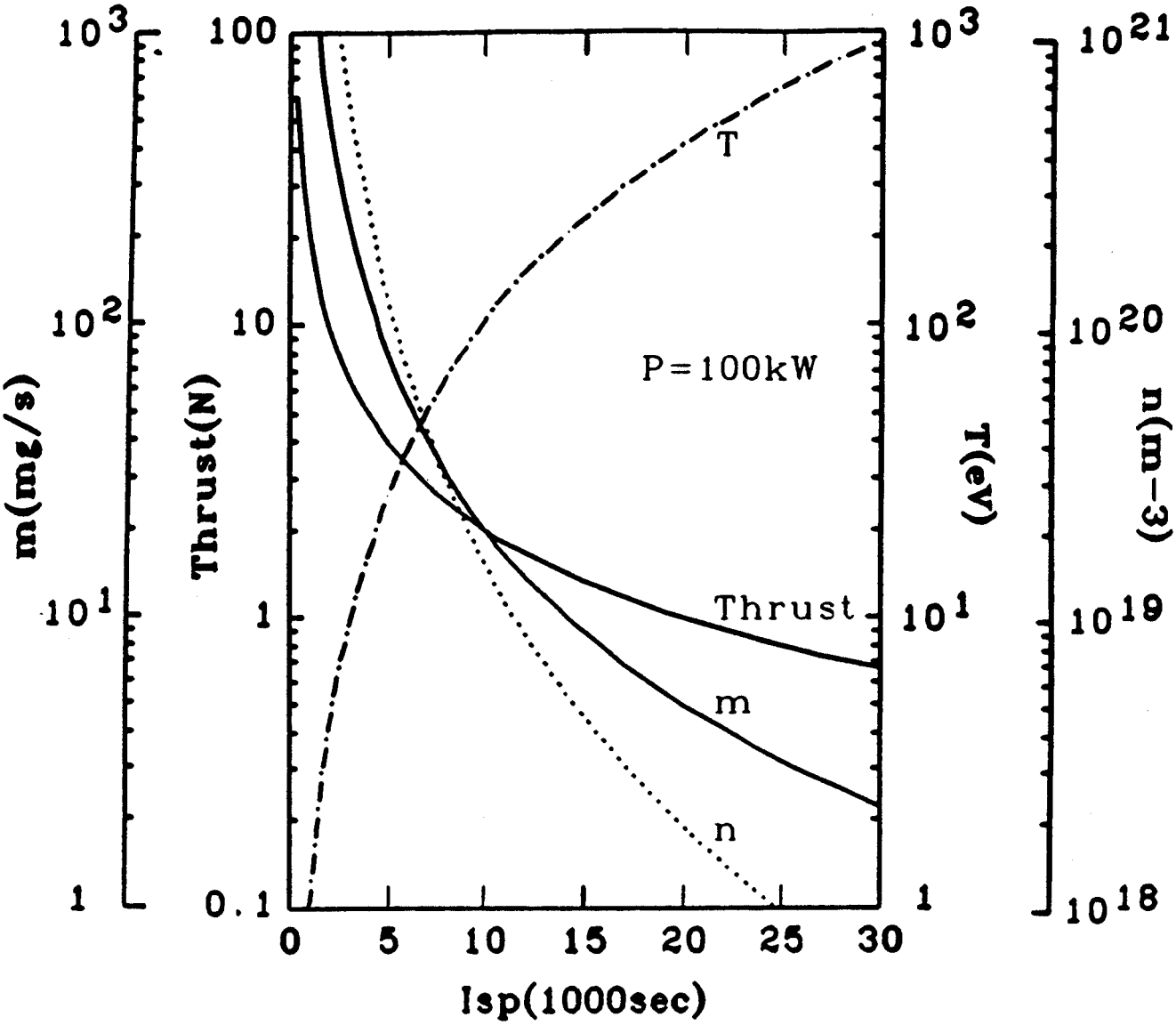

Fig.16: Propulsion parameters,thrust and mass flow as a function of Isp(solid curves, left scale), the corresponding plasma parameters(dashed curves,right scale) at constant power P=100kW.

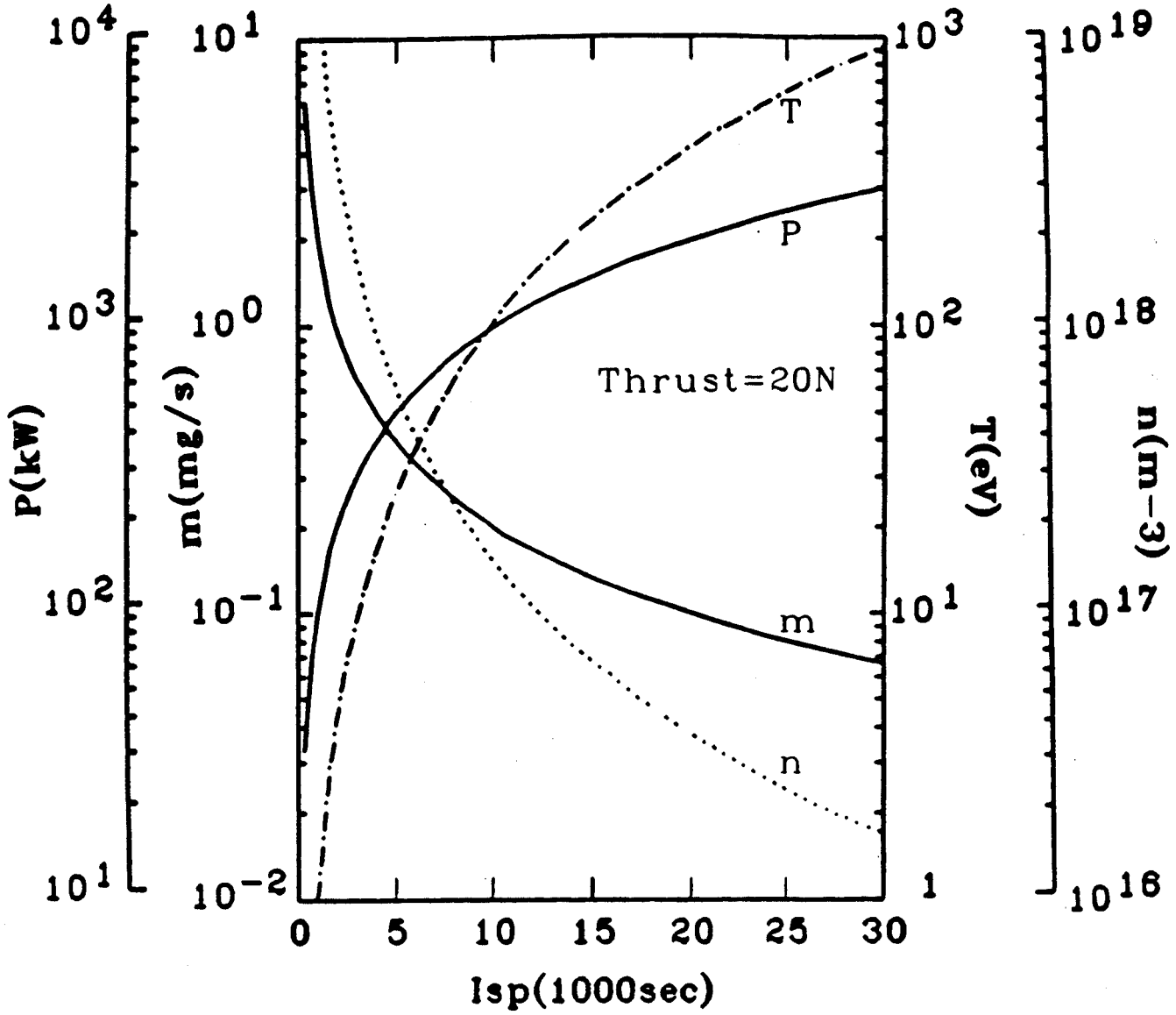

Fig.17: Propulsion parameters, thrust and power (solid curves, left scale) as a function of Isp and the corresponding plasma parameters, temperature and density (dashed curves, right scale) at constant thrust=20 N

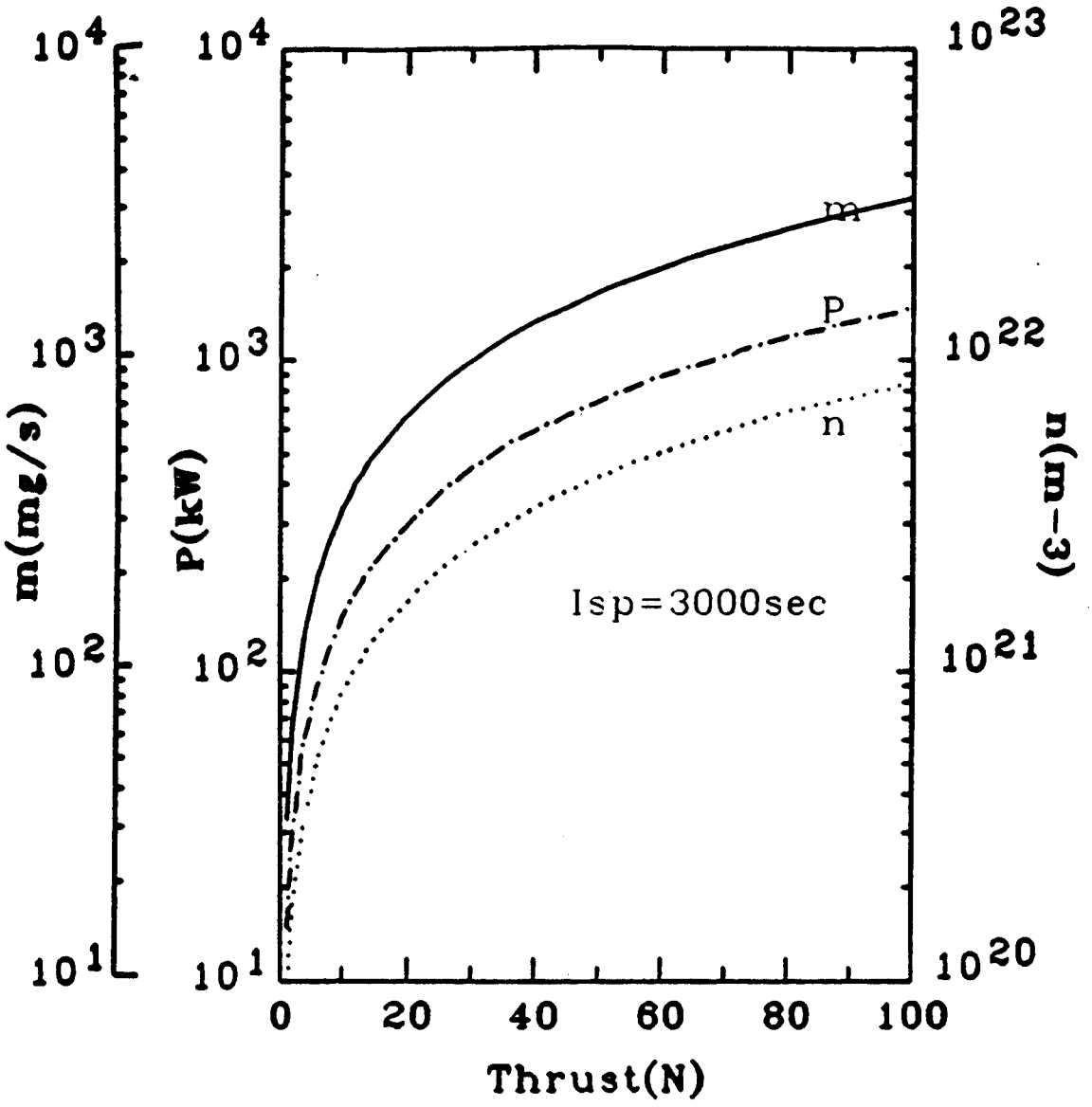

Fig.18: Propulsion parameters, mass flow and P (solid curves, left scale) as a function of thrust and the corresponding plasma parameters(dashed curves, right scale) at constant Isp=3000sec (T=9.39eV).

this concept, the pressure is actually a tensor and should be treated as such. Therefore in the fluid equation one should use $\nabla \cdot p$ instead of ∇p. The viscosity was ignored and should be incorporated in the future. The code should be modified to take this important physics into account and should be continuously generalized to become as realistic as possible.

Experimentally heating the plasma to high temperature has been proven by the large fusion devices. However, the nature of the operation is not the same as for propulsion purposes. For a fusion device one would like to confine the plasma as long as possible and heat the plasma to extremely high temperatures, whereas for a propulsion device, one would like to make the plasma flow at modest temperatures, but at much higher densities. Some other problems such as magnetic detachment and asymmetric operation are important for propulsion, but have never been attempted in fusion research. The entire parameter space shown in Figs. 16, 17 and 18 need to be mapped out by experimental data with a clear understanding of the plasma properties. Although the rf heating of plasma has been studied by researchers in fusion, both theoretically and experimentally, the physics is still not completely understood.

5 Objective and Benefit

The objective and benefit are closely related and described in long and near term below.

The ultimate long term goal and benefit is to develop a variable I_{sp} and thrust rocket propulsion device with power conversion efficiency better than 50%. The I_{sp} can vary from 1,000 sec up to 30,000 sec. The thrust is mainly restricted by the power.

The near term goal is to achieve the plasma conditions (temperature, density and mass flow rate) for the wide propulsion performance characteristics specified in Figs. 16, 17 and 18 and to develop a simplified and reliable control method. The near term benefits are understanding the fundamental physics of heating the plasma with rf power. The device provides a test bed for other advanced propulsion concepts such as anti-matter propulsion, for nozzle studies, for high temperature space material development and for possible space

plasma experiments. Both the computational tool and diagnostic developed in this research can be used in research in other areas such as MPD and arcjet. Therefore the long range specific objectives can be stated in terms of physics and technology as follows.

Physics Objectives

1. To investigate the physics of plasma/neutral interaction in thin, hypersonic boundary layers. Specifically, what is the impact of cold (neutral) gas injection and/or mixing into the exhausted plasma as it pertains to thrust augmentation, thrust efficiency, specific impulse variability and plasma/ magnetic field decoupling as a function of various operating conditions and system configurations?

2. To investigate plasma magnetic field detachment mechanisms in magnetic nozzles. Specifically, what are the conditions under which effective decoupling of the exhausted plasma from the magnetic field lines will take place such that useful thrust may be produced?

3. To investigate the physics of RF and microwave-heated plasmas. Specifically, how to best couple power to the plasma and under what conditions is it more efficient to heat ions over electrons.

4. To investigate the characteristics of tandem mirror configurations operating asymmetrically. Specifically, what the specific impulse (I_{sp}) of the exhausted plasma is for a variety of operating conditions of plasma density and temperature and magnetic field configurations.

Long-Term Technology Objectives

1. To demonstrate the viability of the hybrid plume rocket as a plasma propulsion scheme. Specifically, to obtain a characterization of the operating envelope of such a device.

2. To investigate the technology of magnetic nozzles. Specifically, what fraction of the total kinetic (thermal) energy of the generated plasma can be realized as useful thrust for propulsion?

3. To investigate the operation of a tandem mirror device as a variable I_{sp} plasma rocket.

4. To serve as a pathfinder toward the design and construction of a flight unit to be tested in low Earth orbit.

5. To carry out efficiency studies under a variety of system configurations.

6 Scope of Work for February 1990 to January 1991

The long term objective is to achieve the plasma characteristics for wide propulsion application as shown in Figs. 16, 17 and 18.

As discussed in Section 2.2 the microwave feedthrough is installed at the right end (north end) of the central cell and the rf antenna is in the north end cell as shown in Fig. 19. The rf power heats the plasma ions and creates an electrostatic ambipolar potential ϕ_1 in the north end. A second antenna will be installed in the central cell where the bulk plasma can be heated by a second rf transmitter. Eventually a third antenna will be constructed and installed in the south end. Then the third rf transmitter will be needed to heat the plasma in the south end to create the electrostatic ambipolar potential ϕ_2. This completes the tandem mirror configuration. Many parts of the third transmitter were removed for repairing the other two. Extensive parts and work are required to bring up this transmitter to operation.

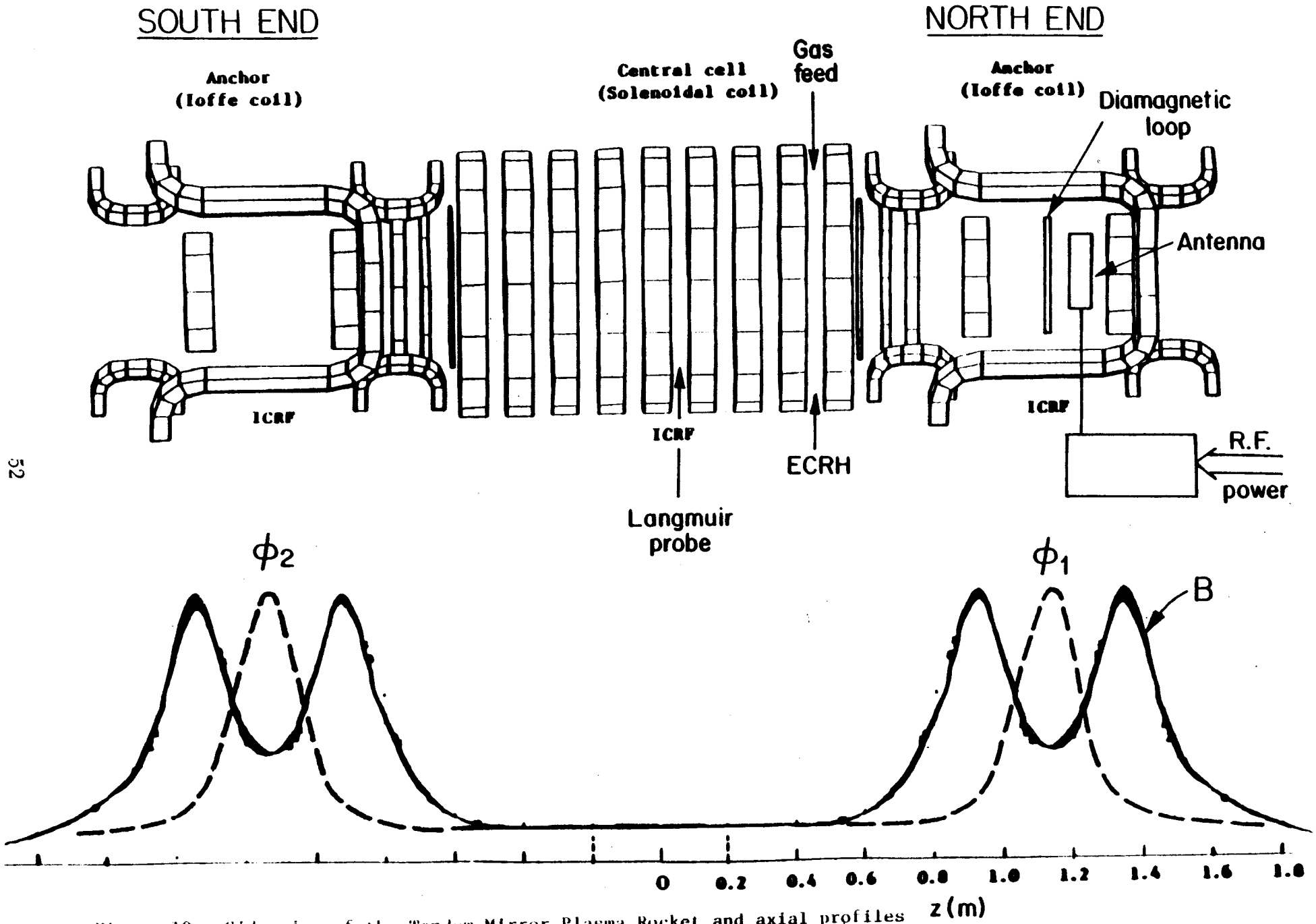

Figure 19. Side view of the Tandem Mirror Plasma Rocket and axial profiles of the magnetic field B and electric potential .

At present we have only Langmuir probes installed in the central cell which can only measure the electron temperature at the cold plasma surface. We need to measure the ion temperature for two reasons. The first reason is that the ions carry the momentum which are the main thrust producing elements. The second reason is that the potentials ϕ_1 and ϕ_2 are proportional to the ion temperature. The proper method for measuring temperature is laser Thomson scattering which is too expensive and complicated. To set up, operate and make measurements with Thomson scattering requires at least a full time scientist. We are going to try to determine the ion temperature from Doppler broadening of radiations produced by helium using a monochromatic spectrometer. It is not a simple task even to make Doppler broadening measurements work. It needs very high time resolution and much faster time scanning than the built-in scanning system. We are planning to use a rotating mirror to disperse the frequency. At present we are lucky to be able to borrow a spectrometer for several months which will allow us to study such a rotating mirror system.

Two diamagnetic loops were installed outside the chamber located at the north end cell and the central cell. The test results indicate that a signal was shielded by the vacuum chamber. Therefore the loops need to be installed in the interior of the chamber. To make such an installation is very complicated. The loop has to be wound inside a tube and be vacuum tight, and it also has to be protected from the plasma. The chamber has to be opened at many locations for the installation. The diamagnetic loop measures the ratio of plasma pressure to magnetic pressure called β

$$\beta = P/(B^2/2\mu) \ . \tag{96}$$

Since the magnetic pressure $B^2/2\mu$ is known, the overall plasma pressure can then be determined

$$P = \beta \left(\frac{B^2}{2\mu} \right) \ . \tag{97}$$

To measure the energy of the ions and electrons in the exhaust we need a retarding field grid energy analyzer. Such an energy anlyzer developed for fusion research is shown in Fig. 20. The electronics for driving the probe includes power supply, functional generators and a multi-channel digitizer. The probe itself is not only expensive but also very complicated and delicate. The probe has to be calibrated with monoenergetic beams.

At present the experimental results were recorded by taking Polaroid pictures from the screen of the oscilloscopes. The picture quality is very poor as seen from Figs. 2 through 4, which makes it difficult to analyze. The use of film turned out to be very expensive. We urgently need to set up the computer data acquisition system. The hardware interface which was obtained without cost was installed and software has to be implemented and tested.

It is not possible to discuss all the diagnostic system and measurements and the data acquisition system. To build, test, calibrate and identify corrrect measurements is a major part of the scientific effort.

The first stage experiment will be carried out with a mirror field of 6 kG, which is about half of the design value and just above the ICRF resonance magnetic field. The mirror coils can be run at room temperature with intermittant cooling. To run at higher fields the coils have to be cooled down to liquid nitrogen temperature. The rf power injection will be started at a low power level (10–20 kW) and short pulse length (10–20 ms). The power level and pulse length will be increased gradually after the plasma properties are fully understood and optimal operating conditions are obtained. Study will be made on the effect on heating with varying gas flow rates, field intensities, and microwave radiation feedthrough locations.

During the course of the heating experiment we will try to study the diamagnetic loop for plasma β measurement and to complete implementation of a computer data acquisition and reduction system. A microwave interferometer will also be installed for plasma density measurement.

More diagnostic equipment is needed. It typically takes at least two months to make a given diagnostic operational and to understand the measurements. In addition to the experimental study the following specific tasks are planned: (1) to study the diamagnetic loop measurements; the loop is outside the chamber and may need to be moved inside the chamber; (2) to acquire a spectrometer to do Doppler broadening measurements for obtaining ion temperature; (3) to construct and install a second antenna in the central cell and to tune the rf transmitter for injecting the power into the central cell; (4) to

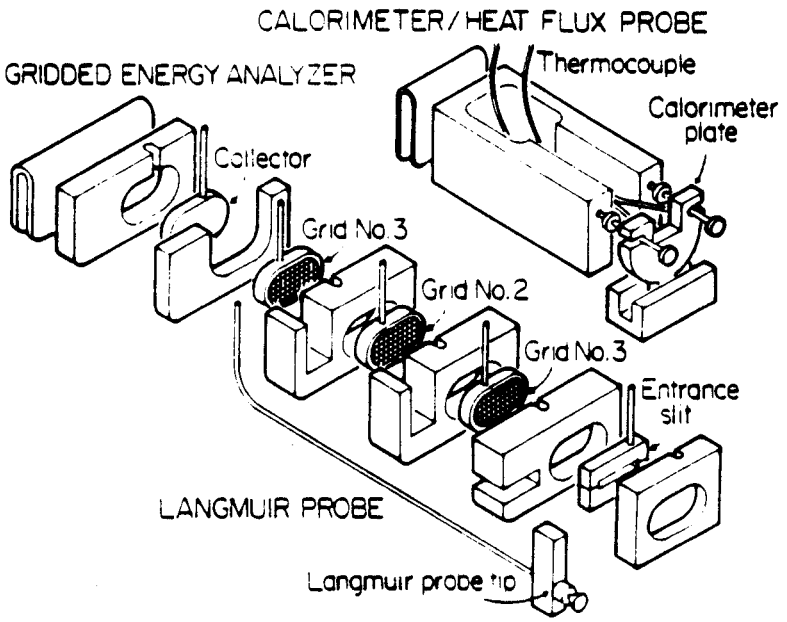

Figur· 20. Trimetric view of a retarding field grid energy analyzer.

carry out heating experiments in both the central cell and the anchor; (5) to make the third rf transmitter operational for heating the other anchor; and (6) to convert the pulsed microwave transmitter to full wave.

7 Instrumentation Requirements (1990)

To understand the plasma properties correctly we need many diagnostic instruments. At present we urgently need the following

1. Langmuir probes

   Langmuir probes will be used to measure the plasma edge density and temperature at various locations. A known profile will be used to project the center conditions. We already have made one set of working probes. We need to build more probes and a power supply to drive the probes.

2. Diamagnetic loop

   A diamagnetic loop will be used to measure the β in the central cell and one of the plugs. β is the ratio of plasma pressure to magnetic field pressure $P/(B^2/2\mu)$. Therefore we can determine the over plasma pressure $P = \beta(B^2/2\mu)$.

3. $\dot{B}$ probe array

   A $\dot{B}$ probe array will be used to monitor magnetic fluctuations and propagation of rf waves. From this we will study the method of improving the efficiency.

4. Bolometer

   A bolometer and electronics will be used to monitor radiation losses.

5. Grid energy analyzer

   A grid energy analyzer and electronics will be used to measure plasma potential in the plug and particle energy at the exhaust from which we can determine the exhaust velocity.

6. Visible light spectrometer

A visible light spectrometer will be used to measure ion temperature from the Doppler broadening of the light.

7. Data acquisition system

   We obtained an agreement to share the data acquisition VAX computer with the fusion energy research groups. The interface hardward and software have been installed. We are testing the operation. However, our CAMAC crater and digitizer are too slow. High speed CAMAC craters and digitizers are needed.

8. Emissive probes to measure plasma potential.

8 Available Facility

The propulsion experimental facility has been set up and is operational. The major equipment is listed in Table 3.

Table 3

Major Equipment

ITEM	RATING	QUANTITY
Tandem Mirror Device		
Turbo Pump	400 liter/sec	2
Microwave	2.4 MHz, 2kW	1
Power Supply	7,000 kW, DC, 5000 amp (5 MW, 2 sec pulse)	2
	18 kW, DC, 600 amp	1
	150 kW, DC, 5000 amp	1
	3 kW, DC, 200 amp	1
RF Transmitter	300 kW, DC, 2-30 MHz	3
Dye Laser		1
Ruby Laser		1
CAMAC Interface		1
Large Vacuum Tank with Pumping System		1

References

1. F. R. Chang, J. L. Fisher, Nuclear Fusion, **22**, No.8 (1982).

2. F. R. Chang, W. A. Krueger, T. F. Yang, AIAA/DBLR/JSASS Int. Electric Propulsion Conference, paper AIAA-85-2049, Alexandria, VA, Sept. 1985.

3. T. F. Yang, R. H. Miller, K. W. Wenzel, W. A. Krueger, AIAA/DBLR/JSASS Int. Electric Propulsion Conference, paper AIAA-85-2054, Alexandria, VA, Sept. 1985.

4. F. R. Chang-Díaz, T. F. Yang, W. A. Krueger, S. Peng, J. Urbahn, X. Yao, D. Griffin, DGLR/AIAA/JSASS, 10th Int. Electric Propulsion Conf., paper DGLR-88-126, Garmisch-Partenkirchen, W. Germany, October 1988.

5. T. F. Yang, F. R. Chang-Díaz, S. Peng, J. Urbahn, X. Yao, AIAA/ASME/SAE/ASEE, 25th Joint Propulsion Conf., paper AIAA-89-2383, Monterey, CA, July 1989.

6. I. H. Hutchinson, "Principles of Plasma Diagnostics," Cambridge University Press, Cambridge, 1st Edition (1987).

7. S. J. Braginskii, Reviews of Plasma Physics, Vol. 1, edited by M. A. Leontovich, New York 1965, p. 205.

8. B. McVey, "Antena User Guide," MIT Plasma Fusion Center Report PFC/RR-84-13 (1984).

9. R. Bruen, J. Conrad, S. Golovato, J. Kesner, R. S. Post et al, "Initial Results from the Tandem Mirror Phaedrus," IAEA 10th Conf. on Plasma Physics and Contr. Nucl. Fus. Res., paper IAEA-CN-3/F-2-3, Vienna (1981).

10. T. D. Shepard, T. D., private communication, 1986.

11. N. T. Lam et al., "Analysis of Dielectric-Filled Waveguide Coupling to Plasmas in the ICRF," IEEE Transaction on Plasma Science, vol. ps-14, No. 3, pp. 271–276, June 1986.

12. G. Schmidt, "Physics of High Temperature Plasmas," Second Edition AP, New York, 1979